

INFORMATION TO USERS

This was produced from a copy of a document sent to us for microfilming. While the most advanced technological means to photograph and reproduce this document have been used, the quality is heavily dependent upon the quality of the material submitted.

The following explanation of techniques is provided to help you understand markings or notations which may appear on this reproduction.

1. The sign or "target" for pages apparently lacking from the document photographed is "Missing Page(s)". If it was possible to obtain the missing page(s) or section, they are spliced into the film along with adjacent pages. This may have necessitated cutting through an image and duplicating adjacent pages to assure you of complete continuity.
2. When an image on the film is obliterated with a round black mark it is an indication that the film inspector noticed either blurred copy because of movement during exposure, or duplicate copy. Unless we meant to delete copyrighted materials that should not have been filmed, you will find a good image of the page in the adjacent frame. If copyrighted materials were deleted you will find a target note listing the pages in the adjacent frame.
3. When a map, drawing or chart, etc., is part of the material being photographed the photographer has followed a definite method in "sectioning" the material. It is customary to begin filming at the upper left hand corner of a large sheet and to continue from left to right in equal sections with small overlaps. If necessary, sectioning is continued again—beginning below the first row and continuing on until complete.
4. For any illustrations that cannot be reproduced satisfactorily by xerography, photographic prints can be purchased at additional cost and tipped into your xerographic copy. Requests can be made to our Dissertations Customer Services Department.
5. Some pages in any document may have indistinct print. In all cases we have filmed the best available copy.

University
Microfilms
International

300 N. ZEEB RD., ANN ARBOR, MI 48106

8219051

Numan, Muhammad Zillulhaq

DIFFUSION AND TRAPPING OF POSITIVE MUONS IN NIOBIUM AND IN
ALUMINUM ALLOYS

The College of William and Mary in Virginia

PH.D. 1982

University
Microfilms
International 300 N. Zeeb Road, Ann Arbor, MI 48106

DIFFUSION AND TRAPPING OF POSITIVE MUONS
IN NIOBIUM AND IN ALUMINUM ALLOYS

A Dissertation

Presented to

The Faculty of the Department of Physics
The College of William and Mary in Virginia

In Partial Fulfillment
Of the Requirements for the Degree of
Doctor of Philosophy

by

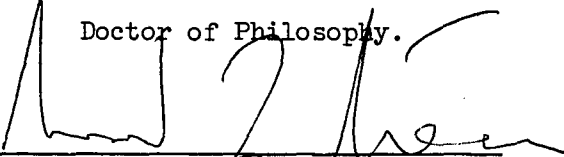
Muhammad Zillulhaq Numan

1982

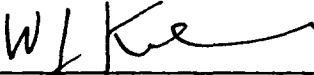
APPROVAL SHEET

This dissertation is submitted in partial fulfillment of
the requirements for the degree of

Doctor of Philosophy.


Muhammad Zillulhaq Numan

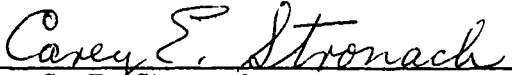
Approved, April 6, 1982


W. J. Kossler, Chairman


K. G. Petzinger


H. E. Schone


M. S. Conradi


C. E. Stronach
Virginia State University

CONTENTS

ACKNOWLEDGEMENTS vii

LIST OF FIGURES viii

LIST OF TABLES xii

ABSTRACT xiv

Chapter

page

I. INTRODUCTION 1

II. MUON SPIN RESONANCE 7

The Probe 8

Muon Properties 8

Muon Production 10

Muon decay	13
Interaction of thermalized muons with matter . .	17
Muonium formation	17
muon location	20
Magnetic interactions	20
The relaxation processes	24
uSR technique	28
Transverse field method	30
Longitudinal field method	34
III. MUON DIFFUSION AND TRAPPING: THEORETICAL BACKGROUND	35
Diffusion in Nb	36
The Kubo-Toyabe model	39
Static muon in zero or low external field . .	39
Stochastic hopping: diffusion & detrapping .	43
The Trapping Model	45
Trapping in zero external field: Petzinger	
model	47
Trapping with low external field	49
Trapping in dilute Al alloys	52
Multiple trap model for the transverse	
relaxation function	52
The Laplace Transform method	55

IV.	EXPERIMENTAL DETAILS	58
	The muon channels	58
	The setup	61
	The cryostat and temperature control	68
	The samples	71
	Data acquisition	73
V.	DATA ANALYSIS	77
	Zero and longitudinal field data in Nb	78
	Transverse field data	82
	Time calibration	83
	The fitting routines	85
VI.	RESULTS AND CONCLUSIONS	87
	Nb studies	87
	Al alloys	93

Appendix

page

A. INVERSION OF LAPLACE TRANSFORMATION USING FOURIER
SERIES 96

REFERENCES 100

ACKNOWLEDGEMENTS

I wish to express my gratitude to the following individuals:

W. J. Kossler, my thesis advisor, for his guidance, encouragement and instructions over the course of this work;

K. G. Petzinger for his theoretical contributions towards and personal interest in the project;

A. T. Fiory and M. Leon for their contributions to the data analysis;

H. E. Schone, M. S. Conradi, and C. E. Stronach for careful reading of the manuscript and for serving on my dissertation committee;

Thea Bartos for helping with the typing.

I would like to thank the SREL and LASL staff for their assistance in carrying out the experiments, the William and Mary Computer Center for their support, and the National Science Foundation for the research grant.

LIST OF FIGURES

<u>Figure</u>	<u>page</u>
1. A schemetic drawing of the transverse Nb data . . .	4
2. Pion and muon decay in center of mass co-ordinates.	15
3. Energy spectrum of positrons from the muon decay . .	15
4. Tetrahedral and octahedral interstitial sites in bcc	21
5. Transverse field uSR setup: schematic	31
6. Longitudinal field uSR setup: schematic	32
7. Transverse depolarization of positive muons in Nb. .	37
8. Transverse depolarization of positive muon in Bi . .	37

9.	Conservation of the z-component of the spin	40
10.	Theoretical Kubo-Toyabe curves for $G_z(t)$	46
11.	Calculated values of $G_z(t)$ obtained from the	51
12.	Layout of LAMPF stopped muon channel	59
13.	Layout of SREL meson channel	62
14.	Transverse field setup	64
15.	Longitudinal field setup	65
16.	Transverse field setup at SREL	67
17.	Electronic logic: LASL experiment	74
18.	Electronic Logic: SREL experiments	76

19.	$G_z(t)$ at 11K and zero external field	106
20.	$G_z(t)$ at 11K and 15 external field	107
21.	$G_z(t)$ at 18.5K and zero external field	108
22.	$G_z(t)$ at 18.5K and 15 external field	109
23.	$G_z(t)$ at 24.3K and zero external field	110
24.	$G_z(t)$ at 24.3K and 15 external field	111
25.	$G_z(t)$ at 46K and zero external field	112
26.	$G_z(t)$ at 77.3K and 15 external field	113
27.	$G_z(t)$ at 77.3K and 15 external field	114
28.	$G_x(t)$ at 11K and 100G transverse field	115
29.	$G_x(t)$ at 18.5K and 100G transverse field	116
30.	$G_x(t)$ at 24.3K and 100G transverse field	117
31.	$G_x(t)$ at 46K and 100G transverse field	118

32.	$G_x(t)$ at 79.3K and 100G transverse field	119
33.	Linewidth parameter α of Al(Si) fitted to a five trap model . .	120
34.	Linewidth parameter α of Al(Ag) fitted to a three trap model .	121
35.	Linewidth parameter α of Al(Mg) fitted to a four trap model . .	122

LIST OF TABLES

<u>Table</u>	<u>page</u>
1. Basic properties of Muon, Proton, and Positron . . .	9
2. uSR facilities around the world	10
3. Temperature control parameters for the Nb experiment	70
4. Variations in parameter values from run to run . . .	81
5. Calibration coefficients for time to channel conversion	85
6. Fitted parameters: Zero, , and <u>l</u> field Nb experiments	89
7. Comparison with earlier work	92

8. Impurity conc., binding energy, and / for Al-alloys . 94

9. Coeffs. of C_v for computing inverse Laplace
transforms 99

ABSTRACT

Zero, longitudinal and transverse magnetic field μ SR has been used to investigate μ^+ diffusion and trapping in Nb. The ambiguity in the interpretation of the 'double humped' temperature dependence of the discussion of how the zero and longitudinal measurements can distinguish between the trapping and detrapping phenomena is presented with μ^+ SR data analysis in mind. Muon mobility is shown to increase monotonically with temperature. The width of the local magnetic field distribution due to Nb nuclear moments and the rate for trapping and detrapping of muons have been measured at several temperatures.

Data from an earlier study of aluminum doped with .1 at % Si, Ag and Mg showing complex structure in the linewidth parameter have been analyzed further using a multi-trap nonequilibrium model to obtain trap concentration, binding energies and diffusion rates for the host and the trap.

DIFFUSION AND TRAPPING OF MUONS IN NIOBIUM
AND IN DILUTE ALUMINUM ALLOYS

Chapter I

INTRODUCTION

The study of the diffusion of positive muons in metals dates back to the pioneering work of Gurevich et al.¹ on Cu. Since then copious research in this field has expanded our understanding of the motion of light interstitial particles in metals. Unanswered questions remain, however, in the general province of impurity or defect trapping and the exact nature of diffusion of this light isotope of hydrogen. In this thesis we shall address one such question, the diffusion of muons in imperfect Nb. The effects of impurities will also be probed via muon diffusion and trapping in dilute Al alloys.

The mobility of a muon depends on its energy, on the temperature of the host, and on the presence of impurities and defects in the crystal. Muons may be localized in traps near the defect centers, or in the bulk of the host material

where the potential energy surface has local minima due to defect induced strain fields (Anderson localization)². Typically muons diffuse rapidly and find traps if these exist. The possibility of coherent band-like propagation of muons has been entertained, particularly at low temperature. However, unless the temperature is very low, and the crystal very pure, an incoherent hopping seem to be the more probable means of diffusion.

In μ^+ SR studies spin polarized muons are stopped in the material to be studied where they precess with the Larmor frequency in the local magnetic field sampled by the muon ensemble. The asymmetric decay of the muons into positrons preferentially in the muon spin direction with a mean lifetime of 2.2 μ s provides the means for investigating the time evolution of the muon spin polarization. A distribution of the magnetic field strength about an average value will result in dephasing of the μ^+ precession and a depolarization rate corresponding to the transverse linewidth in an NMR spectrum.

In conventional transverse field μ^+ SR, stationary muons randomly implanted in a non-magnetic material are depolarized by the surrounding nuclear moments while a mobile muon shows a significant drop in the depolarization rate due to motional narrowing. The presence of trapping centers is re-

flected by complex structure in the temperature dependence of the linewidth parameter. The peaks at different temperatures may represent self-trapping in the host material or trapping at low energy sites in the vicinity of impurities or defects. An indirect measure of host diffusion rate may also be obtained from such data if one assumes that muons are implanted randomly in the sample, and an average muon has $2.2 \mu\text{s}$ to find a trap. The non-equilibrium theories of transverse diffusion, however, cannot resolve certain ambiguities about the diffusion process.

The double-humped behavior (Fig. 1) of the Nb data is a case in point. According to one interpretation muons in this schematic diagram are undergoing thermally activated diffusion; they are weakly bound to a high-concentration trap at point 1, at point 2 many of them are leaving this trap due to thermal agitation showing motional narrowing, at point 3 a lower concentration trap of greater depth inhibits motional narrowing, at point 4 most or all muons are bound to this trap, and finally at point 5 muons are being activated out of these deeper traps. A diametrically opposite interpretation invokes coherent diffusion suggesting that muon mobility increases with decreasing temperature between points 4 and 3, that the hump at point 4 is due to self-trapping in the host material, and that traps are being

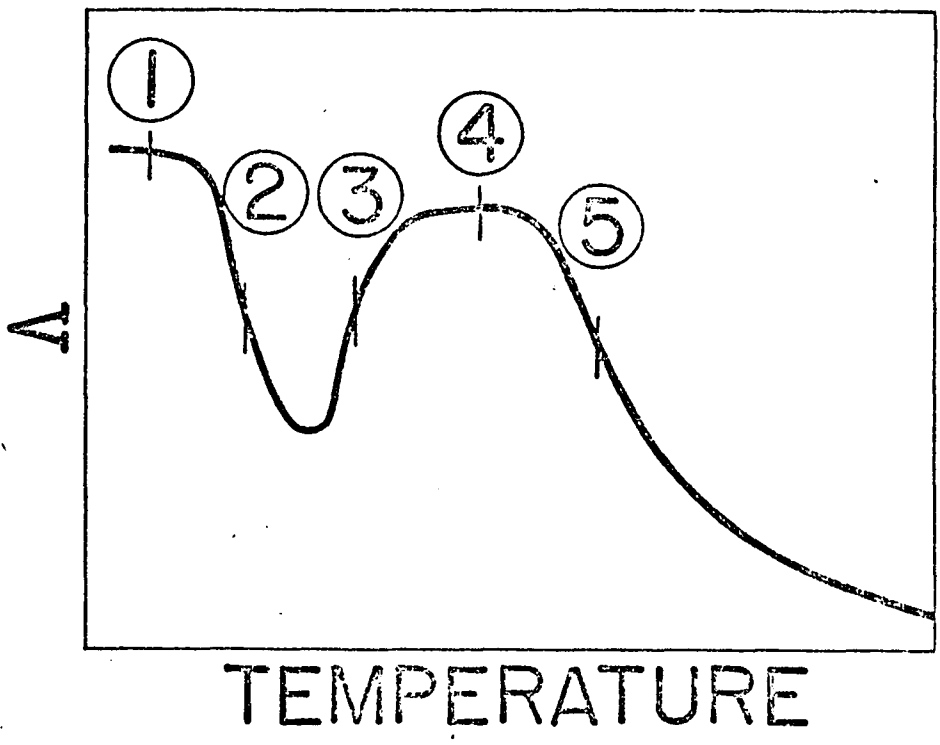


Figure 1: A schematic drawing of the transverse μ b data

reached at points 2 and 1 due to greatly enhanced mobility of the muons.

The settling of this controversy by the use of recently developed methods of zero-field nSR is one of the major topics of this thesis. As has been pointed out by Petzinger³, zero-field measurements can readily distinguish between muons entering traps or escaping from them on the basis of the long time behavior of the relaxation rate. The rates of trapping and detrapping are also amenable to calculation on the basis of existing theories. Our experiments have unambiguously determined the actual diffusion process involved. In addition to the zero field runs, measurements in transverse and in weak longitudinal field were made to extract trapping and detrapping rates independently from the zero field values.

We also have investigated the effect of impurities on fcc Al, which in the pure state is known to show virtually no depolarization over a wide temperature range from 1K to 300K. To understand the multi-peaked linewidth curve seen we have employed a non-equilibrium motional narrowing theory with the Laplace transform approach due to A.T.Fiory to obtain information about trapping rates, trap concentrations and trap binding energies from our data. A similar analysis was originally applied to positron annihilation studies⁵.

Some uncertainties still persist because of the rather complicated nonlinear fitting procedures and the phenomenological nature of the theory behind the method. Here is a field pregnant with potential for both theoretical and experimental exploration, and we intend to pursue a systematic study of such alloys with various concentrations of the impurities over a wide temperature range in future.

In chapter II we discuss the methodology of μ^+ SR in general, proceeding therefrom in chapter III to discuss the motivation and the specific theoretical models that underpin our experiments. The details of the experiments are documented in chapter IV. Chapters V and VI deal with the analysis of the data, followed by an enumeration of results in Chapter VII.

Chapter II

MUON SPIN RESONANCE

Over the past decade, positive muons have been extensively employed to study various aspects of solid state physics including electronic structure of metals, local fields in magnetic materials, low temperature diffusion and trapping by impurities and defects, muonium formation in semiconductors, etc.^{7, 8}. In view of its similarity to NMR, EPR, and ESR the discipline acquired its acronym: μ SR. Excellent reviews of the field exist in the literature⁹⁻¹³. In this chapter we present a brief overview of the fundamentals of μ SR, as a background for the present work.

2.1 THE PROBE

2.1.1 Muon Properties

For solid state purposes, the positive muon is a close kin of the proton, being only one-ninth as massive, and can be treated as a light isotope of hydrogen. It has less in common with its much lighter leptonic counterpart, the positron, which behaves quite differently in many respects-- although in studies of defects and impurities in metals the muon bears some similarities to the latter¹⁴. The absence of a complicated electron core or a quadrupole moment frees μ SR studies from masking effects and competing interactions of the electric field gradients and the magnetic field as encountered in Mossbauer or NMR data analysis. A list of basic properties of positive muons, along with those of protons and positrons, is given in Table I.

TABLE 1

Basic properties of Muon, Proton, and Positron

Particle	Positive muon, μ^+	Proton, p	Positron, e^+
Rest mass	$m_\mu = 206.769 m_e$ $= 0.01261 m_p$ $= 105.659 \text{ MeV}/c$	$m_p = 1836.152 m_e$ $= 1.6726 \cdot 10^{-27} \text{ kg}$ $= 938.28 \text{ MeV}/c$	$m_e = 0.91095$ $\times 10^{-30} \text{ kg}$ $= 0.51100 \text{ MeV}/c$
Spin I	1/2	1/2	1/2
Magnetic moment μ	$\mu_\mu = 1.001166 (m_e/m_\mu) \mu_B$ $= 3.18334 \mu_p$ $= 4.4905 \cdot 10^{-26} \text{ JT}^{-1}$	$\mu_p = 2.7928 \mu_N$ $= 1.4106 \cdot 10^{-26} \text{ JT}^{-1}$	$\mu_e = 1.001160 \mu_B$ $= 658.2107 \mu_p$
Gyromag. ratio γ ($\text{rad} \cdot \text{s}^{-1} \text{ T}^{-1}$)	$= 8.5161 \cdot 10^8$	$= 2.6752 \cdot 10^8$	$= 1.7608 \cdot 10^{11}$
Quad moment Q	0	0	0
Lifetime ($= \tau_{1/2} / \ln 2$)	$= 2.197 \cdot 10^{-6} \text{ s}$	stable	stable, annihilating with e^- in 10^{-10} to 10^{-7} s
Atom	Muonium $\text{Mu} = \mu^+ + e^-$	Hydrogen $\text{H} = p + e^-$	Positronium $\text{Ps} = e^+ + e^-$
Bohr magneton $\mu_B = e\hbar/2m_e$	$= 9.2741 \cdot 10^{-24} \text{ JT}^{-1}$		
Nuclear magneton $\mu_N = e\hbar/2m_p$	$= 5.0508 \cdot 10^{-27} \text{ JT}^{-1}$		

2.1.2 Muon Production

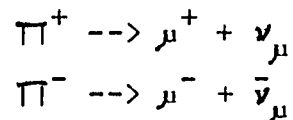
Muon beams used for uSR are currently generated at medium energy (500-800 MeV) proton accelerators also known as 'meson factories'. Table 2 lists the major facilities where μ SR experiments have so far been performed, as well as one proposed to start operation in 1982.

TABLE 2

uSR facilities around the world:

Facility	Proton current μ A	μ^+ momentum MeV/c	μ^+ flux $s^{-1} cm^{-2}$
CERN, Geneva, Switz.	4	124	50
TRIUMF, Vancouver, B.C.	20	50	60
SIN, Villigen, Switz.	80	120	2×10^5
LAMPF, Los Alamos, N.M.	300	130	8×10^2
BNL, Brookhaven, N.Y.	2.10^{12} protons per pulse	200	7×10^7 μ^+ per 10^{12} p

At the meson factories, muons are produced by the decay of charged pions according to the following schemes:



The lifetime of charged pions in the above reactions is:

$$t_{\pi^{\pm}} = 2.60 \cdot 10^{-8} \text{ s},$$

corresponding to a pion mean free path of 6.4m at $p_{\pi} = 200 \text{ MeV}/c$ ($v=0.82 c$). In the pion rest system the muons have a momentum of $29.79 \text{ MeV}/c$ corresponding to a kinetic energy of 4.1192 MeV . Muons in the above equation are 100% longitudinally polarized, with their spin directed opposite to their momentum (fig.2), which arises from the requirement of momentum and angular momentum conservation and the fact that the muon neutrino has a negative helicity.

The pion decays in flight in the so-called muon channels. In the laboratory frame of reference, the muons accepted by the solenoid come from the forward or backward cone relative to the pion momentum in the pion rest frame. The momenta of the muons emitted in the forward and the backward direction in the laboratory frame are given by¹³:

$$p_{\mu}^c = p_{\pi}^c \frac{m_{\pi}^2 + m_{\mu}^2}{2m_{\pi}^2} \pm \frac{m_{\pi}^2 - m_{\mu}^2}{2m_{\pi}^2} \left[m_{\pi}^2 c^4 + p_{\pi}^2 c^2 \right]^{1/2} \quad (2.1)$$

For a typical pion momentum of $p_{\pi} = 200 \text{ MeV}/c$ muons in the forward cone have a higher momentum of $209.37 \text{ MeV}/c$, while those in the backward cone have a lower momentum of $105.26 \text{ MeV}/c$. At the end of the channel bending magnets are used for beam separation and momentum selection. Extraction of muon beams by momentum selection in the laboratory system leads to the so called kinematic depolarization¹⁷, which arises from the fact that the collimated muon beam exits at a slight incline to the pion beam, retaining about 80-85% of its polarization. The muons emitted in the forward direction are backward polarized, and vice versa. Typically, the backward polarized beam is the more intense but the forward polarized beam has less background contamination and produces reduced straggling of the muons in the target.

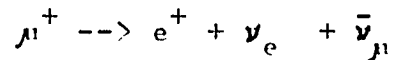
The energy of the muon beam is usually reduced appropriately to stop the muons inside the sample by passing the beam through light materials (water, polyethylene, etc.). The polarized muons are then stopped in the material to be investigated (Fig.2). On entering the sample, muons thermalize very rapidly by scattering with the electrons. In non-metals muons typically capture an electron to form muonium in the final stage of thermalization; ensuing hyperfine interactions contribute to some loss in polarization. Thermalization (i.e. drop of the kinetic energy to $\sim 3k_B T/2$) in

metals takes place within about 10^{-13} s to 10^{-12} s, a time scale very short compared to the muon lifetime, and results in a negligible change in polarization.

The negative muon is captured by the atoms in a solid, and cascades down through the various shells losing much of its polarization, thus reducing its effectiveness in investigating solid state properties. A status report on negative muon spin resonance (μ^- SR) can be found in ref.30. The rest of our discussion will be confined to positive muons.

2.1.3 Muon decay

The main decay mode of the positive muon is:



The two component Dirac theory of the neutrinos, with a weak interaction Hamiltonian consisting only of the vector and the axial vector coupling constants, describes the above parity non-conserving muon decay²⁷ very well. According to this theory, neglecting the positron rest mass compared to its momentum, $p_e = m_e c$, and the small QED corrections, one may write the probability per unit time of positron emission into a solid angle $d\Omega$ in a direction forming an angle θ with the u spin direction as:

$$dW(x, \theta, t) / d\Omega dx dt$$

$$=(3-2x)/(2n_{t\mu}) [1 + P \cdot a(x) \cos\theta] x^2 e^{-t/t_{\mu}} \quad (2.2)$$

Here P is the degree of polarization of the decaying muons. x is the positron kinetic energy in units of its maximum possible energy:

$$x = E(e^+) / E_{\max}(e^+) \quad (2.3)$$

The maximum k.e. is

$$E_{\max} = \frac{m_{\mu} c^2}{2} - m_e c^2 \left(1 - \frac{m_e}{m_{\mu}} \right) = 52.320 \text{ MeV} \quad (2.4)$$

The asymmetry parameter

$$a(x) = (2x - 1)/(3 - 2x) \quad (2.5)$$

is strongly energy dependent as is shown in fig.3. It is negative for $E(e^+) < E_{\max}(e^+)/2$ and positive for $E(e^+) > E_{\max}(e^+)/2$. At $E(e^+) = E_{\max}(e^+)/2$, $a(x)$ takes a maximum value of one.

The efficiency $\epsilon(x)$ with which the positrons are detected is not constant over the entire energy range, and the observed distribution probability takes the form:

$$dW(\theta)/d\Omega = \int [dW(\theta, x)/dx d\Omega] \epsilon(x) dx$$

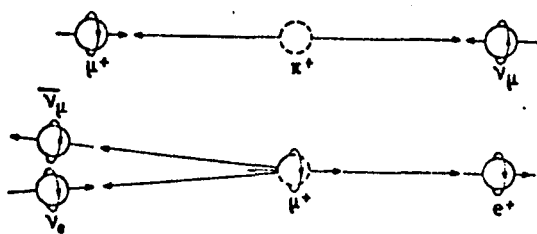


Figure 2: Pion and muon decay in center of mass coordinates.

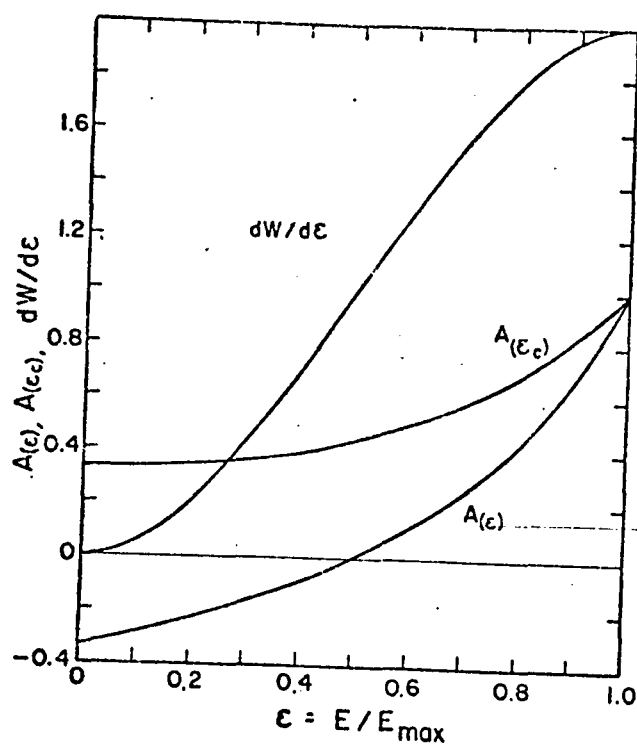


Figure 3: Energy spectrum of positrons from the muon decay and energy dependence of the asymmetry parameter.

$$= \bar{\epsilon} (1 + P \cdot a_{\text{eff}} \cos\theta) \quad (2.6)$$

If all positrons are detected with equal efficiency one gets an average value of a_{eff} :

$$\bar{a}_{\text{eff}} = 1/3.$$

It is possible to eliminate the low energy positrons, for which the asymmetry parameter has the opposite sign, by insertion of absorbers between the target and the detectors-- thus increasing the measured asymmetry. This, however, would have the adverse effect of reducing the counting rate. In practice, asymmetry is somewhat reduced due to the finite detection angle, resulting in effective values in the range .22-.30. Note that the spatial anisotropy of positron emission is preferentially in the muon spin direction, a key fact used to detect the polarization of muons in solids.

2.2 INTERACTION OF THERMALIZED MUONS WITH MATTER

2.2.1 Muonium formation

After thermalization the positive muon is destined for one of the two possibilities: to form or not to form a muonium (Mu), hydrogen-like atoms with muon core formed by capturing an electron from nearby atoms or a narrow conduction band. Muonium formation is evidenced in various insulators and semiconductors, but in metals the screening by conduction electrons almost invariably prevent any formation of bound states.

The cross-section for muonium formation depends on muon speed v , and has maximum around

$$v = a \Delta E_{\text{ion}} / h,$$

where a is of the order of magnitude of atomic radii,

ΔE_{ion} is the difference in ionization energies of Mu ($=13.530\text{eV}$) and of the atom that had donated the electron. The maximum cross-section is of the order of magnitude of the geometric cross-section of these atoms.

With the direction of motion of the muon as the axis of quantization, either a triplet or a singlet muonium may be formed depending on whether the electron spin is parallel or anti-parallel to the muon spin. In non-ferromagnetic mater-

ials both the states will have equal probability of formation. In the absence of external perturbation, the muonium in the triplet state would maintain its polarization but those in the singlet state would exchange their spin direction with the electron with a hyperfine frequency:

$$\omega_{\text{hf}} = \frac{8 \mu_0 \mu_e \mu_u}{3 \pi \hbar a_\mu^3} = 2.804 \cdot 10^{10} \text{ s}^{-1} \quad (2.7)$$

The time scale of the above depolarization process is long compared to the thermalization time for muons, but small compared to muon life time. Thus muons in the singlet muonium state should appear fully depolarized and formation of thermalized muonium should lead to a reduction of the original muon polarization by at least one-half in non-ferromagnetic materials. The fast depolarization observed in many non-metals, attributed to this process, makes a measurement of this depolarization rate almost impossible.

In a weak local transverse field, \underline{B} the triplet muonium precesses with the Larmor frequency,

$$\omega_{\text{Mu}} = \mu_{\text{Mu}} B / \hbar,$$

where μ_{Mu} is the muonium magnetic moment, dominated by the larger magnetic moment of the electron, and

$$\mu_{\text{Mu}} / \hbar = 1.394 \text{ MHz/G.}$$

The singlet muonium polarization oscillates about zero value at high frequency, as in the field-free case, resulting in a rapid hyperfine oscillation superimposed on a slower muonium precession. This permits direct measurement of the hyperfine interaction.

In metals the above-mentioned loss of polarization by at least one-half has not been reported. This, of course, is not surprising since in metals large electron spin-flip rates arising from the exchange interaction between any 'muonium electron' and the conduction electrons is shown to be comparable to the hyperfine frequency at all accessible temperatures.¹¹ The question of detection of muonium has been studied in detail by Grebinnik, et al.^{28,29}, and Gorelkin and Smilga³¹. The latter proposed a measurement of the muon polarization in superconductors with zero nuclear spin, sufficiently below the transition temperature. Here the conduction electrons will be mostly paired and dipole-dipole interaction between muons and nuclei will also be absent, making any reduction of the polarization to one-half due to muonium formation to be observable. No such experiment has yet been reported. For a detailed discussion of Muonium spin resonance (MSR) and muonium chemistry see the review articles mentioned earlier in this chapter.

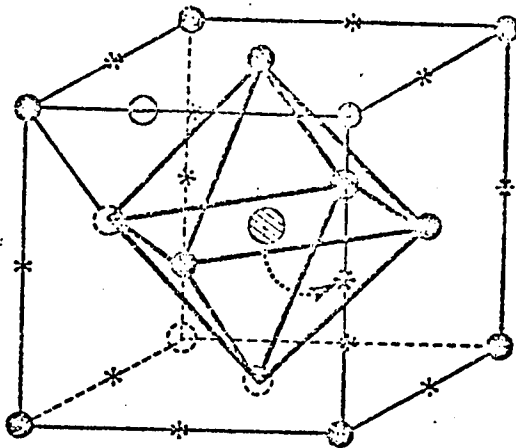
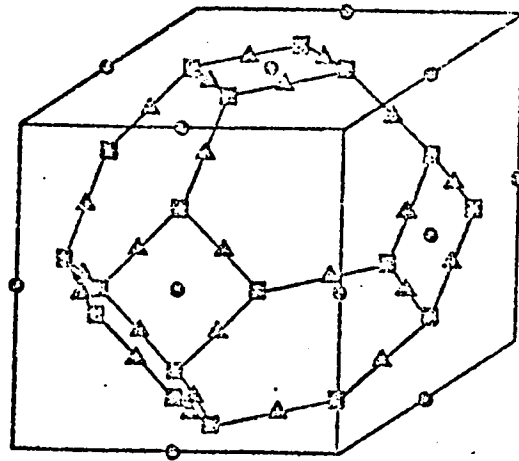
2.2.2 muon location

The dominant interaction of the muons is that with the electrostatic fields in the material which determine what sites muons can occupy. In metals muons occupy an interstitial position, as is the case with the hydrogen nuclei, or are trapped at vacancies, dislocations, or other defect centers. Two of the most attractive candidates for muon location, tetrahedral and octahedral interstitial sites for b.c.c. and f.c.c. crystals are shown in fig.4. It is possible to determine experimentally which particular interstice a muon prefers in a crystalline lattice. To understand this one has first to consider the magnetic interactions of the muon and the transverse relaxation process, as will be discussed below.

2.2.3 Magnetic interactions

The principal source of information in uSR is the interaction of the magnetic moment of the thermalized muon with the magnetic field it samples. In a time independent magnetic field \vec{B}_μ at the muon location the magnetic moment and the spin of the muon rotate with the angular frequency (Larmor precession):

b.c.c. crystals.
Circles: octahedral,
squares: tetrahedral.



f.c.c. crystals.
Shaded circle: octahedral,
Open circle: tetrahedral.

Figure 4: Tetrahedral and octahedral interstitial sites in bcc and fcc crystals.

$$\omega_{\mu} = \gamma_{\mu} B_{\mu} \quad (2.8)$$

yielding information about the local fields, particularly in the ferromagnetic materials.

Another outcome of this interaction, alluded to earlier in connection with the muonium atom, is the decay of the initial polarization of the muons. As in NMR, a distinction should be made between the longitudinal and the transverse relaxation. The first involves a reversal of the muon spin in a Zeeman field B_1 parallel (or antiparallel) to the μ^+ spin polarization, requiring an energy transfer between the spin system and the lattice. This process is also known as 'spin-lattice relaxation'. On the other hand, the transverse relaxation takes place if the magnetic field B_{μ} at the muon site has a spatially inhomogeneous component perpendicular to the muon polarization. The phase coherence of the precession, eqn.(2.8), would then be lost gradually as some spins will rotate faster or slower than the mean frequency. Transverse depolarization involves no exchange of energy and is also referred to as 'spin-phase relaxation'.

The various magnetic interactions to which the μ^+ may be subjected with or without accompanying relaxation of the muon spin polarization are enumerated below:

1. The dipole-dipole interaction between the magnetic moment of the muon, $\underline{\mu}_\mu$ and the nuclear magnetin moments $\underline{\mu}_j$, of the ions of the solid, located at \underline{r}_j with respect to the muon is given by the Hamiltonian

$$H_{dip} = \frac{\mu_0}{4} \sum_j \left[\frac{\underline{\mu}_\mu \cdot \underline{\mu}_j}{r_j^3} - \frac{3(\underline{\mu}_\mu \cdot \underline{r}_j)(\underline{\mu}_j \cdot \underline{r}_j)}{r_j^5} \right] \quad (2.9)$$

This interaction is the major contributor to the u^+ -spin relaxation, especially in metals with large nuclear gyromagnetic ratios.

2. The interaction between muons and electron magnetic moments is also given by a Hamiltonian of the above form, when electron moments concentrate on the atom sites, and are denoted by \underline{u}_j at atomic locations \underline{r}_j . Conduction electrons with a finite electron spin density $\rho_{spin}(0)$ at the muon site prohibit direct use of the eqn.(2.8) because $r_j \rightarrow 0$. Taking the proper limit, the resulting interaction Hamiltonian is found to be:

$$H_{Fermi} = -(4\mu_0/3)\mu_\mu \rho_{spin}(0) \quad (2.10)$$

where μ_e is the electron magnetic moment, and $-2\rho_{\text{spin}}(0)$ is the electron magnetization at the muon location. The above interaction is the Fermi contact interaction.

3. Time independent local fields that are same for all μ^+ locations include a) homogeneous external fields, b) demagnetizing fields, $B_{\text{dem}} = -NM$ (M = the bulk magnetization density), in elliptical ferromagnetic samples, and c) in ferromagnetic samples with crystallographically equivalent muon locations--the contact field B_{Fermi} , the residual dipolar field B'_{dip} within a Lorentz sphere, and the Lorentz field, $B_L = (4/3)M_{\text{domain}}$. Such fields do not contribute to any relaxation, longitudinal or transverse.

2.2.4 The relaxation processes

Theoretically, the transverse relaxation function $G_x(t)$ is given by:

$$G_x(t) = \langle \sigma_x(t) \sigma_x(0) \rangle$$

where x is the direction of muon polarization at $t=0$, σ_x is the Pauli spin operator, and $\langle \dots \rangle$ represents an ensemble

average over implanted muons in a frame rotating with the Larmor frequency of the muons about the external field direction. The corresponding longitudinal relaxation function is defined as:

$$G_z(t) = \langle \sigma_z(t) \sigma_z(0) \rangle.$$

In the presence of a strong external magnetic field, the transverse relaxation of the muon spin polarization arising from the dipolar interaction of the muon with the nuclear spins (eqn. 2.9) can be calculated with the following assumptions: a) Interaction between the magnetic moments of muons is absent. b) The gyromagnetic ratio of the muons is large compared to those of the nuclei. Thus, in non-ferromagnetic samples, the muon spin precession frequency $\omega_\mu = \gamma_\mu B_{\text{appl}}$ is much larger than the nuclear spin precession frequency $\omega_I = \gamma_I B_{\text{appl}}$. c) The applied field must be much greater than the local field generated by the nuclear magnetic moments. d) The interaction energy of the electrical field gradient generated by the muons at the nuclear sites with a nuclear quadrupole moment is small compared to the Zeeman energy of the nuclei in the applied field.

In the absence of muon motion, the depolarization is approximately Gaussian:

$$G_x(t) = G_x(0) \exp(-\Delta^2 t^2 / 2) \quad (2.11)$$

$$\text{where } \Delta^2 = \frac{1}{3} I(I+1)h^2 \gamma_u^2 \gamma_I^2 \sum \frac{(1-3\cos^2\theta_j)^2}{r_j^6} \quad (2.12)$$

In (2.12), r_j is the distance between the j th nuclear spin and the muon, and θ_j is the polar angle between the direction of the applied field and the vector connecting the muon site and the j th spin. This result was first obtained by Van Vleck in connection with the line broadening of NMR spectra. Δ is strongly dependent on the crystal orientation and the muon site. A comparison between the calculated values of Δ^2 with the measured value of the same for different crystallographic orientation allows site determination for the interstitial muon. Note, though, that the expression in eqn.(2.12) for Δ^2 is an overestimation of the second moment since the outward displacement of the neighboring ions due to the electrostatic repulsion by the muons as well as the finite overlap of the muon wave function³³ with the nuclear site or its non-spherical nature⁴⁰ are not included in the calculation.

In the presence of stochastic hopping with a correlation time t_c , one obtains:

$$G_x(t) = G_x(0) \exp(-\Delta^2 t_c^2 [\exp(-(t/t_c) - 1 + t/t_c)]) \quad (2.13)$$

This is the well known Abragam formula⁶, which goes over to eqn.(2.11) in the limit $\Delta t_c \gg 1$. In the case of fast diffusion, $\Delta t_c \ll 1$, this leads to an exponential decay,

$$G_x(t) = G_x(0) e^{-\lambda t} \quad (2.14)$$

with $\lambda = \Delta^2 t_c$. This slower decay of polarization is the counterpart of motional narrowing of resonance lines in NMR.

The longitudinal relaxation in the presence of a field B_1 that splits the muon spin-up and spin-down states into two levels differing by a Zeeman energy

$$\Delta E = 2\mu_\mu B_1 = \hbar w_\mu, \quad (2.15)$$

where w_μ is the spin precession frequency, can be seen to take an exponential form from a simple model. If W_\downarrow and W_\uparrow are the downward and upward transition probabilities, then the population of the two levels, n_+ and n_- , are governed by the rate equations:

$$dn_+/dt = W_\downarrow n_- - W_\uparrow n_+ \quad (2.16a)$$

$$dn_-/dt = W_\downarrow n_- + W_\uparrow n_+ \quad (2.16b)$$

From eqns.(2.16) one can see that longitudinal relaxation,

$$G_z(t) = (n_+ - n_-)/(n_+ + n_-), \quad (2.17)$$

from this very simple model takes an exponential form:

$$G_z(t) = G_z(0) \exp(-\lambda t) \quad (2.18)$$

with $\lambda = W_{\uparrow} + W_{\downarrow}$.

In the absence of external field and muon diffusion, $G_z(t)$ shows some unique features. A detailed discussion of the zero field depolarization will be deferred until the next chapter.

2.3 USR TECHNIQUE

In uSR studies one primarily measures the distribution of decay positrons as a function of elapsed muon life-time for an ensemble of stopped muons at certain angles (usually 0° and 90°) with respect to the beam direction. A clock (e.g. a time to amplitude converter) is started when a muon stops in the sample, and stopped when a decay positron is detected by a scintillator array. The time interval resolution is set electronically to typically 10^{-9} sec, and varied by binning during analysis. Events are collected one at a time and a histogram of counts against time is accumulated. The distribution can generally be expressed by the following formula:

$$N(t) = N_0 \exp(-t/t_{\mu}) \left[1 + P \cdot a_{\text{eff}} \cdot G(t) \cos \theta_0 \right] + \text{bgd} \quad (2.20)$$

where $t=t_1-t_0$, t_0 being the time of muon's entry into the sample and t_1 , that of its decay. The angle θ_0 represents the angle between the detector telescope and the muon spin direction. In the presence of a transverse field, this angle would oscillate with time, providing the frequency of muon precession inside the sample. The effective anisotropy constant a_{eff} takes into account the reduction of anisotropy due to geometrical effects of the detector telescopes and unmeasured fast depolarization effects which are sample dependent. $G(t)$ represents the relaxation function which contains much of the solid state information that we will be dealing with in the following chapters. It is usually parameterized to obtain longitudinal or transverse relaxation times, T_1 and T_2 , a hopping rate for a diffusing muon, or a correlation time, etc. as the case may be. B_{gd} represents the background due to random events and N_0 is a normalization factor, proportional to the total number of stopped muons and the geometry and efficiency of the e^+ detectors.

There are essentially two different set-ups that are used in uSR depending on the direction of the external magnetic field applied to the sample. They are known as the transverse and the longitudinal (or the forward-backward) techniques. Experiments under zero external field can be treated as a special case of either.

2.3.1 Transverse field method

In transverse field geometry, a C-magnet or a Helmholtz coil provides an external field perpendicular to the beam direction. A typical detector setup for this case is shown in Fig.5. The B2.M.F coincidence represents a muon stop in the sample and starts a clock (TAC); a subsequent positron detected at the forward detector F or the annular detector A provides the stop signal.

Due to the Larmor precession of the muons, θ_0 in equation (2.20) should be replaced by $\omega_u t + \phi$, where ω_u is the muon precession frequency,

$$\omega_{\mu} = 2\pi f = 2\pi B_{\mu} \times 13.55 \text{kHz/G}, \quad (2.21)$$

and ϕ is a phase parameter consisting of (a) the angle between the telescope axis and the mean polarization of the stopped muon, (b) a medium-dependent phase shift due to pre-thermalization fast processes, and (c) experimental uncertainties in t_0 . The data collected as forward and backward histograms are thus fitted to the function:

$$N(\phi, t) = N_0 \left[\exp(-t/t_u) \{ 1 + A.G_X(t) \cdot \cos(\omega t + \phi) \} + Bgr \right] \quad (2.22)$$

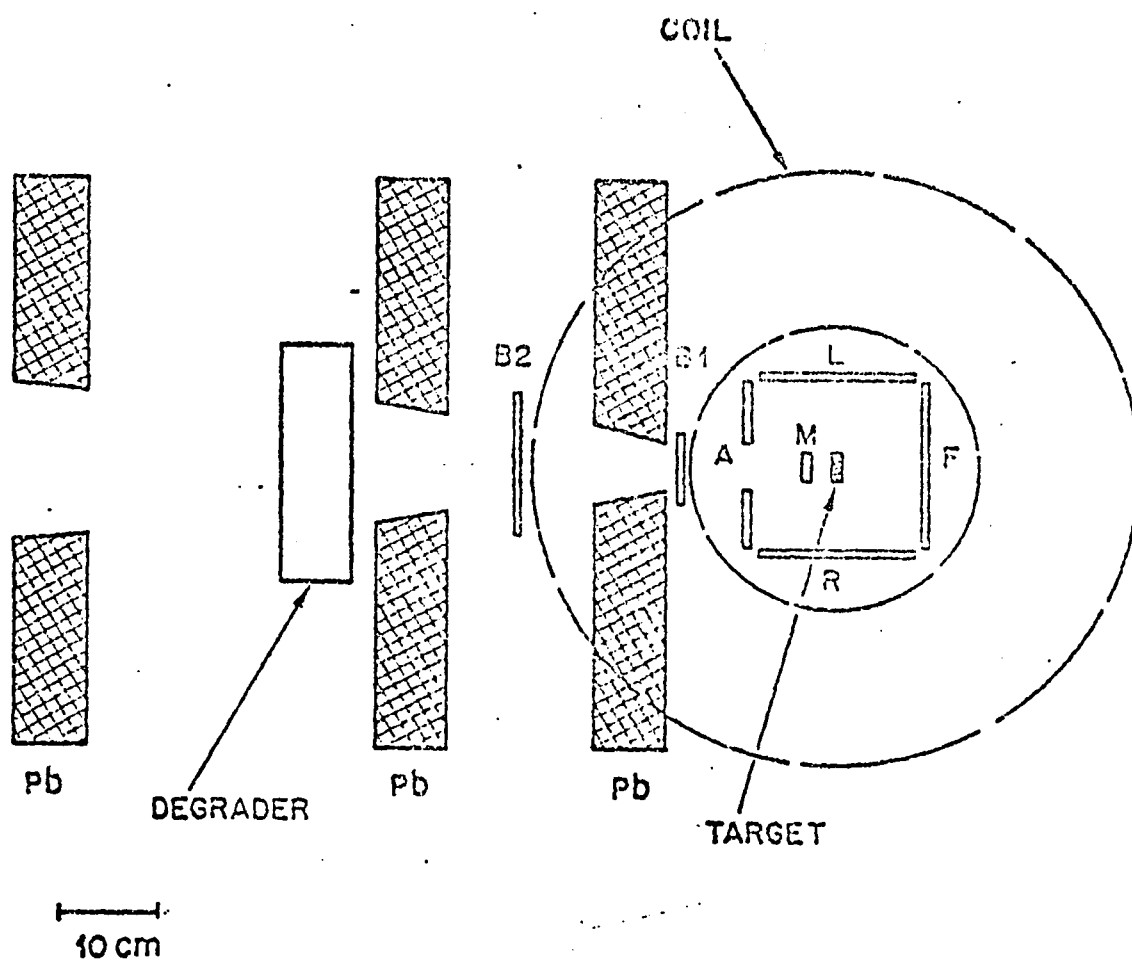


Figure 5: Transverse field uSD setup: schematic

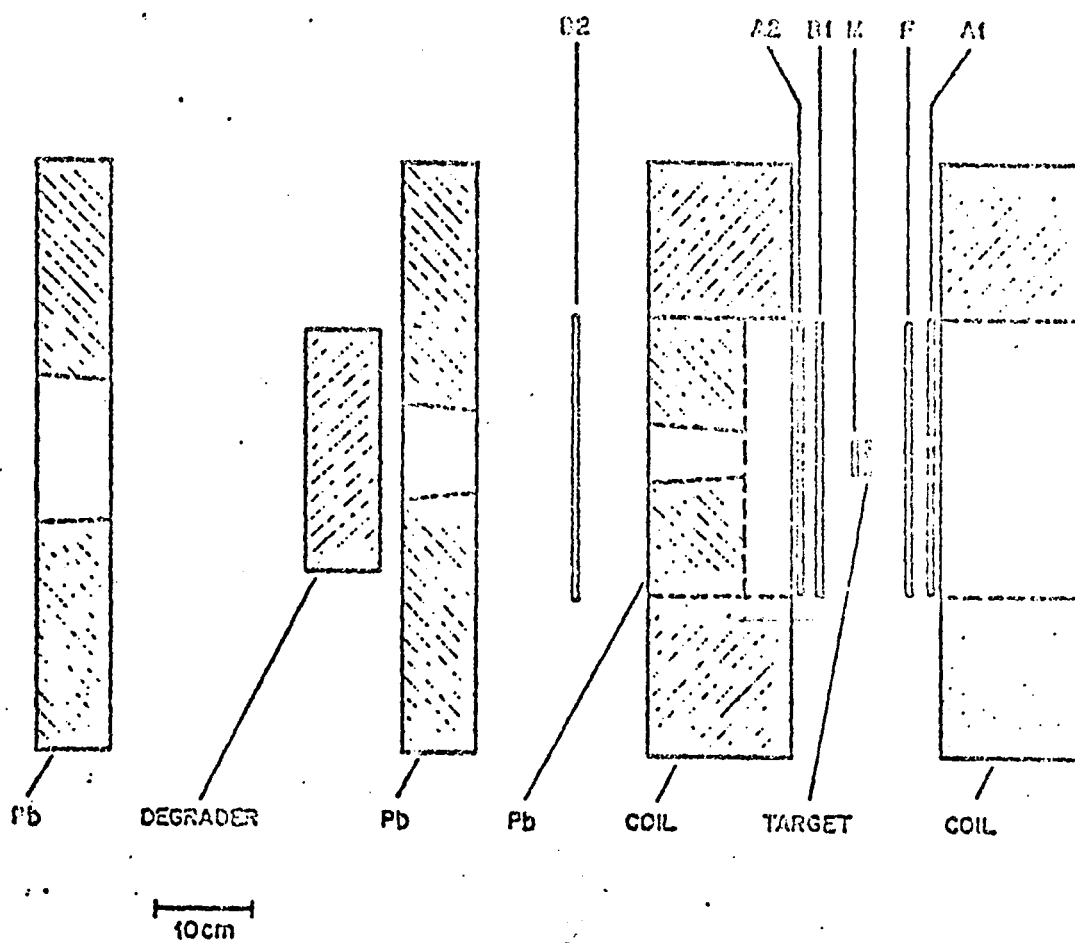


Figure 6: Longitudinal field uSR setup: schematic

In this equation, w actually represents the average precession frequency with a distribution $g(w)$, such that

$$G_x(t) \cos(\bar{w}t + \phi) = \int g(w) \cdot \cos(wt + \phi) dw$$

$G_x(t)$ can be approximated by Gaussian or exponential decay function, e.g.,

$$G_x(t) = \exp(-\lambda t) \quad (2.23)$$

In general, distinct precession frequencies corresponding to several non-equivalent muon sites with differing B fields may exist in the sample. Then one must replace $G_x(t) \cos(wt + \phi)$ by:

$$\sum_i f_i G_x^i(t) \cos(w_i t + \phi_i)$$

where f_i is the fraction of muons precessing at frequency w_i . A simple Fourier analysis of the histogram after removing the background and the exponential decay due to muon lifetime will reveal such peaks in the w distribution. The relaxation function associated with each w value can be obtained from the shape and the width of the individual peaks.

2.3.2 Longitudinal field method

In the longitudinal field method the magnetic field is applied along the muon spin direction using Helmholtz coils. A typical setup is shown in fig. 6. Here B2.B1.M. \bar{F} coincidence denotes a stopped muon; a subsequent signal in the forward or the backward annular detectors determines an event. Numbers of events in the forward and the backward detectors, after background subtraction, can be written as:

$$N'_f = \alpha N_0 e^{-t/t_\mu} [1 + P a_f G_z(t)] \quad (2.24a)$$

$$N'_b = N_0 e^{-t/t_\mu} [1 - P a_b G_z(t)] \quad (2.24b)$$

From the above equations, $G_z(t)$ is given by:

$$G_z(t) = (N'_f - \alpha N'_b) / (P a_b N'_f + \alpha P a_f N'_b) \quad (2.25)$$

This relaxation function can then be fitted to an appropriate form as discussed in section 2.2.4.

Chapter III

MUON DIFFUSION AND TRAPPING: THEORETICAL BACKGROUND

A series of experiments in both transverse and longitudinal geometry was performed in 1981 at the Stopped Muon Channel of the Clinton P. Anderson Meson Physics Facility (LAMPF) to determine the nature of interstitial diffusion and trapping by impurities of μ^+ in crystalline Nb where conventional transverse uSR studies were not conclusive. Our experiments have unambiguously established the diffusion mechanism over the temperature region of interest.

In the first part of this chapter we present the motivation for the above experiments from the theoretical vantage point, elaborating our models in some detail. Then we shall discuss a non-equilibrium theory involving multiple trap sites applicable to the dilute Al-alloy data collected at the Space Radiation Effect Laboratories (SREL) in 1978. The

Laplace transform method of data analysis employed here will also be discussed in this connection.

3.1 DIFFUSION IN NB

Transverse field depolarization studies of bcc Nb demonstrate an unusual pattern over the temperature range of 10K-100K (fig.7) ^{18, 19}. At 10K and 45K the linewidth parameter λ (2.14) forms a plateau with a dip in-between at 20K and an eventual fall-off around 73K.

Similar behavior has also been noted in the case of Ri ²⁰ (fig.8). The anomaly is apparently due to impurities in the metal that produce traps for the muons; but the actual mechanism is not uniquely determined from these transverse experiments. Two different interpretations have been proposed to explain this phenomena. Gurevich at al. proposed coherent diffusion and band-like propagation of muons in the region between the high temperature plateau and the dip, the former being explained as a result of slow mobility through the host interstitial sites. The coherent limit of the small polaron model at low temperature predicts a monotonically decreasing diffusion rate-- or, increased linewidth-- with increase in temperature. The low temperature peak in this interpretation represents depolarization due to trap-

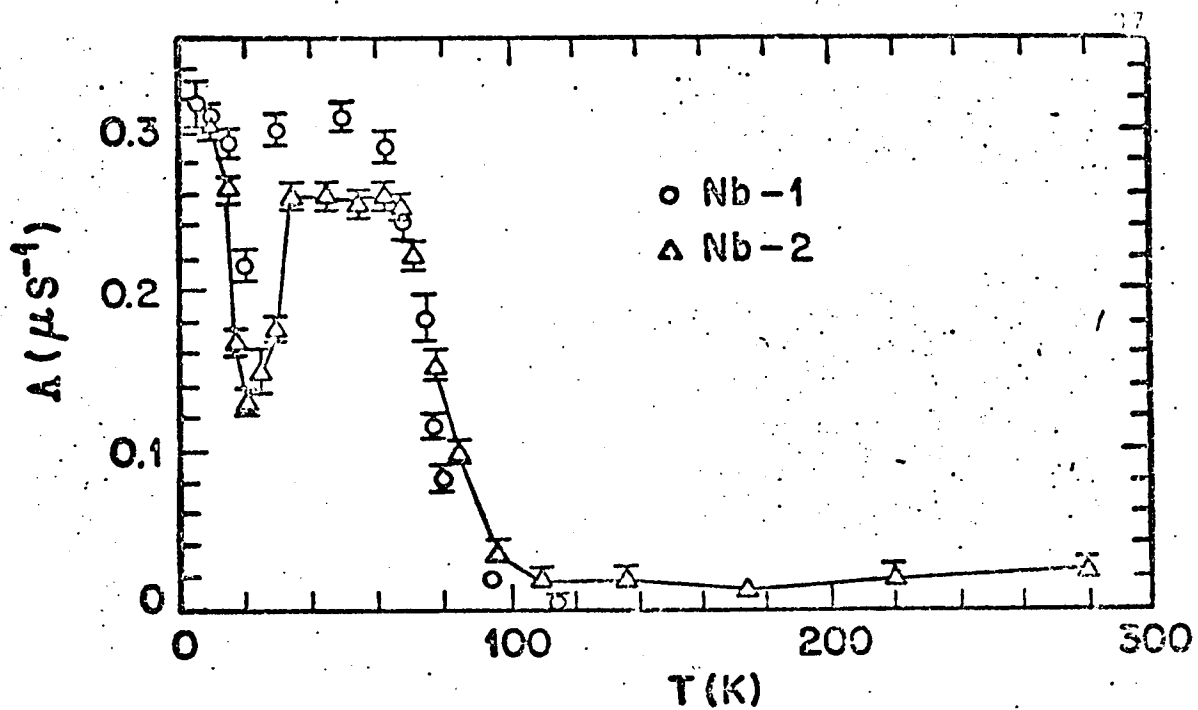


Figure 7: Transverse depolarization of positive muons in Nb. Experiment done at SIN by Birnbaum et al.

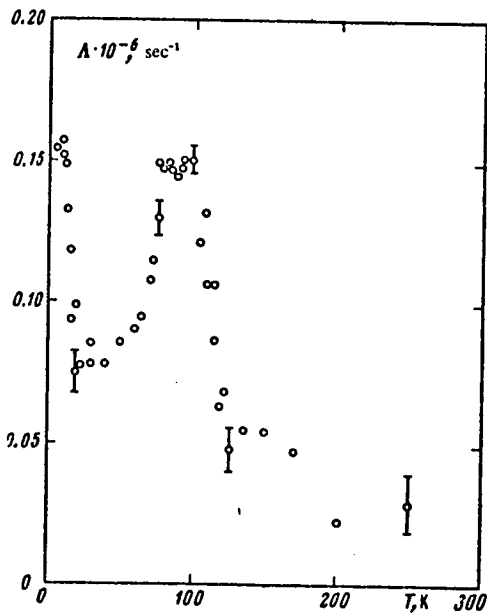


Figure 8: Transverse depolarization of positive muon in Bi. Experiment done at JINR by Grebinnik et al.

ping at impurities. This is a result of enhanced mobility with the drop in the temperature.

The second explanation, due to Petzinger^{3,4}, discredits band-like propagation in view of the random strain present in the lattice. According to this theory muons (in the Nb experiment) are captured by two types of traps of different concentration and depth at the two plateaus; the slope on the low temperature side represents motional narrowing as detrapping from one type of impurities (Ta) ensues with increase in temperature. The other slope then represents the onset of trapping by the second type of impurities (C,O). A similar interpretation would apply to Bi data, with host and impurity plateaus labelled inversely from the previous paragraph.

We set out to distinguish between these two possibilities by longitudinal forward-backward studies of Nb. The form that the longitudinal relaxation function takes when initially non-equilibrium (i.e., randomly distributed in the host) muons relax to traps is qualitatively different from that taken when depolarization is due to detrapping. In the first case the depolarization parameter asymptotically approaches one-third of its initial value, while in the second case it goes to zero in that limit. Over the time range of interest, these functions tend to be rather complicated; but

computer aided numerical methods can employ them very unambiguously in analysing the experimental data. A discussion of the two models is given in some detail in the following sections.

3.2 THE KUBO-TOYABE MODEL

Kubo and Toyabe²¹ worked out the form assumed by the relaxation function for zero and low external fields. These results have been applied by Yamazaki et al.²² to μSR , and also by Hayano et al.^{23, 24} who developed a parallel theory of diffusion.

3.2.1 Static muon in zero or low external field

Consider first the case of zero external field. Let \underline{H} be the local field at a muon stop site. For a spin initially along the z-axis (the direction of the beam transport), the time evolution of its z-component is:

$$\sigma_z(t) = \sigma_z(0) [\cos^2\theta + \sin^2\theta \cos(\gamma_u H t)] \quad (3.1)$$

where θ is the angle between the z-axis and the \underline{H} direction (Fig.9).

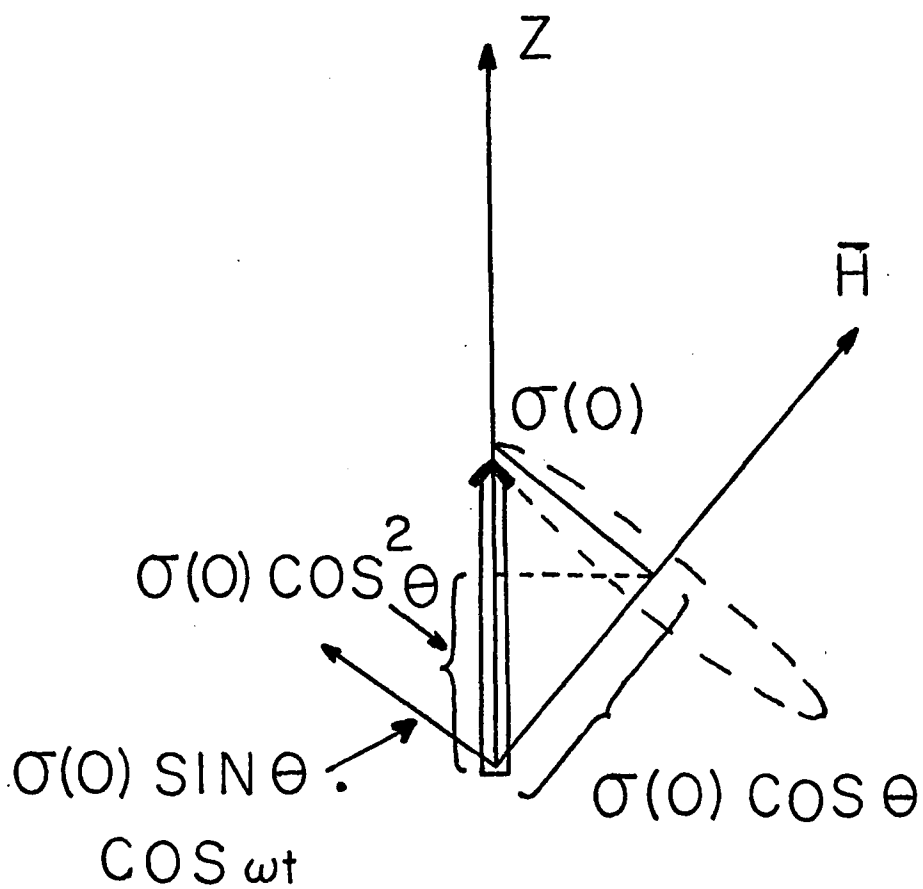


Figure 9: Conservation of the z-component of the spin of the static muon.

Assume the random fields are isotropic and the distribution function for each component can be represented by a Gaussian (which implies a Gaussian-Markovian process):

$$P(H_i) = \frac{Y_\mu}{(2\pi)^{1/2} \Delta} \exp\left(-\frac{Y_\mu^2 H_i^2}{2\Delta^2}\right) \quad i=x,y,z \quad (3.2)$$

where Δ^2/Y_μ^2 represent the second moment of the distribution:

$$\Delta^2/Y_\mu^2 = \langle H_x^2 \rangle = \langle H_y^2 \rangle = \langle H_z^2 \rangle \quad (3.3)$$

The longitudinal relaxation function $G_z(t)$ is the statistical average of $\sigma_z(t)$

$$G_z(t) = \iiint \sigma_z(t) P(H_x) P(H_y) P(H_z) dH_x dH_y dH_z \quad (3.4)$$

$$= 1/3 + 2/3 \cdot (1 - \Delta^2 t^2) \exp(-\Delta^2 t^2/2) = g_z(t) \quad (3.5)$$

In the small t limit $G_z(t)$ goes as $\exp(-\Delta^2 t^2)$ as opposed to $G_x(t)$, which in the static case falls as $\exp(-\Delta^2 t^2/2)$.

This is one added advantage of the forward-backward method over the transverse relaxation studies considering the short muon life-time.

The above relation is the Kubo-Toyabe expression for the static muon relaxation function in zero external field.

When a small field H_0 is present, $P(H_z)$ should be modified:

$$P(H_z) = \frac{\gamma_{\mu}}{(2\pi)^{1/2} \Delta} \exp\left(- \frac{\gamma_{\mu}^2 (H_z - H_0)^2}{2 \Delta^2} \right) \quad (3.6)$$

and the statistical average of eqn.(3.4) becomes,

$$g_z(t) = 1 - \frac{2\Delta^2}{\omega_0^2} \left[1 - \exp(-\Delta^2 t^2 / 2) \cos(\omega_0 t) \right] + \frac{2\Delta^4}{\omega_0^3} \int_0^t \exp(-\Delta^2 t'^2 / 2) \times \sin(\omega_0 t') dt' \quad (3.7)$$

where $\omega_0 = \gamma_{\mu} H_0$. It can be seen from eqn.(3.5) that the asymptotic value of the static, zero-field, forward-backward asymmetry is 1/3; this can also be understood physically from eqn.(3.1), taking the average of the z-component of $O(t)$. In case of finite field corresponding recovery is larger than 1/3 and approaches 1 as the field increases. As $t \rightarrow \infty$, (3.7) gives:

$$\begin{aligned}
 g_z(\infty) &= 1 - \frac{2\Delta^2}{w_0^2} + \frac{2\Delta^3}{w_0^3} \int_0^{\infty} \exp\left(-\frac{1}{2}u^2\right) \cdot \sin\left(\frac{w_0}{\Delta}u\right) du \\
 &= 1 - \frac{2\Delta^2}{w_0^2} + \frac{2\Delta^3}{w_0^3} \cdot \frac{w_0^2}{2\Delta^2} \int_0^{w_0/\Delta} \exp\left(-\frac{u^2}{2}\right) du \quad (3.8)
 \end{aligned}$$

using: $\int_0^{\infty} e^{-at^2} \sin(2xt) dt = \frac{1}{\sqrt{a}} e^{-x^2/a} \int_0^{x/\sqrt{a}} e^{-t^2} dt, \text{ Re } a > 0.$

3.2.2 Stochastic hopping: diffusion & detrapping

When a muon jumps from site to site with a mean hopping frequency ν , sampling local fields that are uncorrelated to each other, a Markovian strong collision model²¹ describes the process. In this model, time evolution of $G_z(t)$ comes from muons that were stationary over the interval t , and those that underwent n jumps:²⁴

$$G_z(t) = \sum_{n=0}^{\infty} g_z^{(n)}(t) \quad (3.9)$$

where $g_z^{(0)}(t) = e^{-\nu t} g_z(t)$

experienced no jumps until time t ,

$$(1) \quad g_z(t) = v \int_0^{\infty} dt' e^{-v(t-t')} g_z(t-t') e^{-vt'} g_z(t') \quad (3.10)$$

represents a muon that jumped at time t' ($0 < t' < t$), etc., and e^{-vt} is the probability that the muon did not jump until time t .

Taking the Laplace Transform of eqn.(3.9), one gets

$$F_z(s) = \int_0^{\infty} G_z(t) \cdot e^{-st} dt \quad (3.11)$$

$$= \sum_{n=0}^{\infty} v^n f_z^{(n)}(s+v) = \frac{f_z(s+v)}{1 - v f_z(s+v)} \quad (3.12)$$

where

$$\begin{aligned} f_z(s) &= \int_0^{\infty} g_z(t) \cdot e^{-st} dt \\ &= \frac{1}{3s} + \frac{2s}{3\Delta} \left(1 - s \int dt e^{-\Delta^2 t^2 / 2 - st} \right) \end{aligned} \quad (3.13)$$

In the presence of a field, $f_z(s)$ becomes:

$$f_z(s) = \frac{1}{s} - \frac{2\Delta^2}{\omega_0^2 s} + \frac{2\Delta^2}{\omega_0^2} \cdot \left\{ e^{-\Delta^2 t^2/2 - st} \cos(\omega_0 t) \right\} + \frac{2\Delta^4}{s\omega_0^3} \cdot \left\{ e^{-\Delta^2 t^2/2} \sin(\omega_0 t) \right\} \quad (3.14)$$

$G_z(t)$ can be computed by numerical inversion of its Laplace Transform using Fourier series expansion (Appendix A). Fig 10 shows some curves of $G_z(t)$ for both zero and low external field.

3.3 THE TRAPPING MODEL

The theory of Kubo and Toyabe has been extended by Pétzinger to treat the non-equilibrium problem of trapping²⁵. In the following we present the trapping model in its essentials.

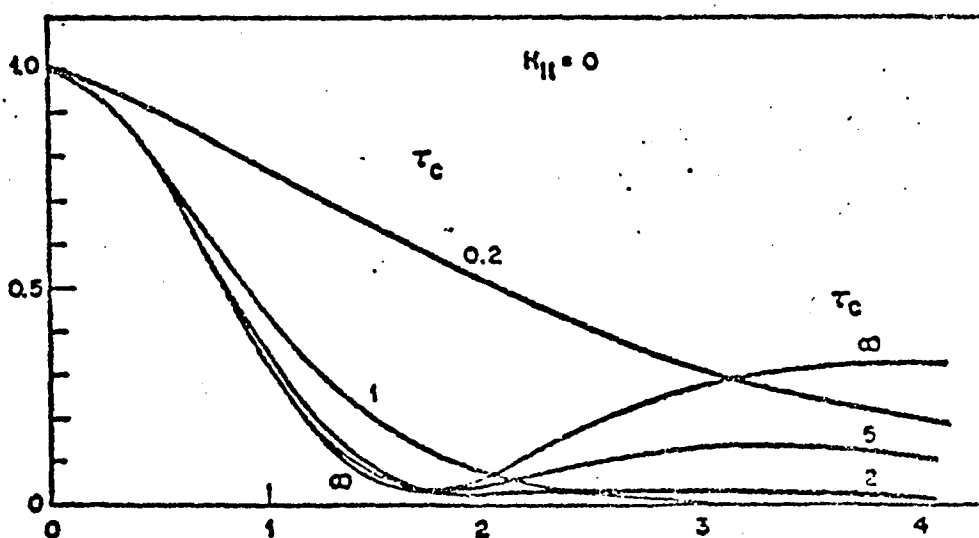
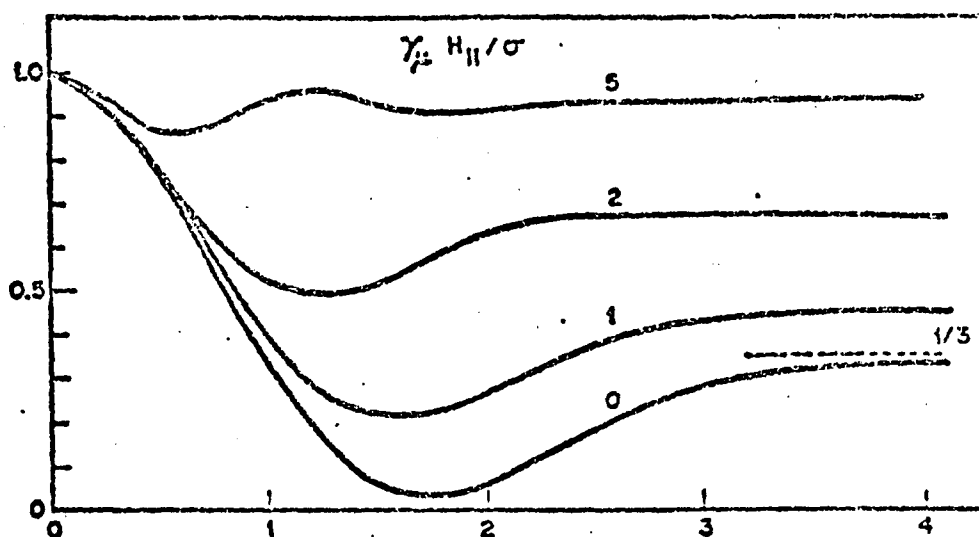


Figure 10: Theoretical Kubo-Toyabe curves for $G_z(t)$ at zero and low longitudinal fields.

3.3.1 Trapping in zero external field: Petzinger model

Consider a temperature regime where (a) depolarization is essentially due to traps, (b) contribution from other sites is negligible due to motional narrowing, and (c) there is no detrapping once the muon is trapped.

The muon spin operator σ obeys the equation of motion:

$$d\sigma/dt = \sum_i \bar{w}_i \times \sigma \quad n_i(t)$$

where w_i is the static precession frequency at the i 'th site of the lattice, and $n_i(t)$ is the occupation number for that site. Since we consider depolarization from only one type of trap site the subscript i can be dropped from the above equation. Now,

$$\begin{aligned} G_z(t) &= \langle \sigma_z(t) \sigma_z(0) \rangle \\ &= T \langle \cos^2 \theta + \sin^2 \theta \cos(\int_0^t w n(t') dt') \rangle \end{aligned} \quad (3.15)$$

where θ is the angle between the initial spin direction and \bar{w} (z-direction), and T is the time ordering operator. With the nonequilibrium probability of finding the muon at site j as Q_j and after averaging over the direction (but not the magnitude) of \bar{w} , one has:

$$G(z) = T \left\langle \sum_j G_j \left\langle |j| \left[\frac{1}{3} + \frac{2}{3} \cos w \int_0^t n(t') dt' \right] |j| \right\rangle \right\rangle \quad (3.16)$$

$$= \left\langle 1 - \frac{2}{3} w \int_0^t \sin w(t-t') N(t') dt' \right\rangle,$$

where $N(t')$ is the probability of trap occupation at time t' . For uniform initial site occupation probability, its value is found to be³⁸:

$$N(t) = 1 - (1 - c)e^{-rt} = 1 - e^{-rt} \quad (3.17)$$

where, $c \ll 1$ is the trap concentration and r is the rate of relaxation to trap sites. After averaging w over a gaussian distribution with $\langle w^2 \rangle = 3\Delta^2$, one obtains Petzinger's result³:

$$G_z(t) = \frac{1}{3} + \frac{2}{3} r^{-rt} + \frac{2}{3} r \int_0^t e^{-r(t-t')} (1 - \Delta^2 t'^2) \exp(-\Delta^2 t'^2 / 2) dt' \quad (3.18)$$

In the limit $r/\Delta \gg 1$, equation (3.18) approaches the Kubo-Toyabe result (3.5), while for $r/\Delta \ll 1$,

$$G_z(t) \rightarrow \frac{1}{3} + \frac{2}{3} e^{-rt}.$$

Note that in either case the asymptotic value of $G_z(t)$ approaches $1/3$, in clear contrast to the detrapping result of an asymptotically vanishing value for the same.

3.3.2 Trapping with low external field

In this section we present a generalised treatment of trapping in a parallel formalism that includes effects of external magnetic field²⁶. Under the assumptions of the previous section the depolarization as a function of time is given quite generally by:

$$G(t) = e^{-rt} g_0(t) + r \int dt' g_1(t-t') \cdot g_0(t') \quad (3.19)$$

for transverse, longitudinal, or zero field case, where $g_0(t)$ is the polarization in the free state and $g_1(t)$ that in the trapped state. For extremely rapid hopping in the non-trapping sites $g_0(t)=1$; if the depolarization from these sites is not negligible, one can approximate $g_0(t)$ by

$$g_0 = \exp(-\lambda t)$$

so that eqn.(3.19) becomes:

$$G(t) = e^{-r't} + r \int dt' e^{-r't'} g_1(t-t') \quad (3.20)$$

where $r' = r + \lambda$. For the trapped state, in the presence of a transverse field such that $\Delta/w \ll 1$, one has:

$$g_1(\mathbf{t}) = \exp(-\Delta^2 t^2 / 2)$$

while for the longitudinal (zero and low field) case $g_1(t)$ is given by $g_2(t)$ of eqn.(3.7). Finally for the transverse case:

$$G_x(t) = e^{-vt} \left\{ 1 + v \int dt' \exp(-t'^2/2 + vt') \right\} \quad (3.21)$$

and for the longitudinal case:

$$G_z(t) = e^{-r't} \left\{ 1 + r \int_0^t dt' \left[e^{r't'} \left(1 - 2 \left(\frac{\Delta}{w} \right)^2 \left\{ 1 - \exp(-\Delta^2 t'^2 / 2) \cos(wt') \right\} \right) + \frac{2}{r} \frac{\Delta}{w} (e^{r't} - e^{r't'}) \exp(-\Delta^2 t'^2 / 2) \sin(wt') \right] \right\} \quad (3.22)$$

The above equation goes over to Petzinger's relation (3.18) when w and λ are set equal to zero.

These functions can easily be computed by evaluating the integrals numerically using Simpson's rule. Some typical curves of the trapping model are shown in Fig.11 .

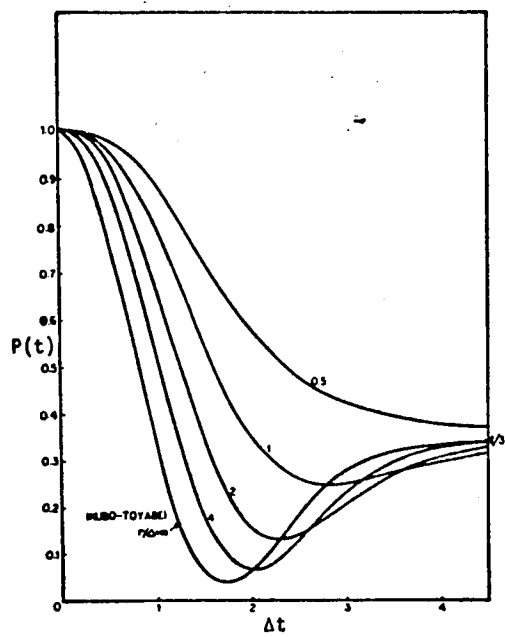


Figure 11: Calculated values of $G_z(t)$ obtained from the trapping model of Petzinger for zero field.

3.4 TRAPPING IN DILUTE AL ALLOYS

The transverse field studies of the fcc metal Al doped with 0.1 at.% of Mg, Si, and Ag undertaken at SREL by our group offered a wealth of complex structure in the temperature dependence of the depolarization rate. A similar study of Al(Cu) seemed to indicate a variety of trapping sites, probably clusters of impurities or impurity-vacancy complexes³⁹.

In analysing the data we applied a multiple trapping model for the high field transverse relaxation function developed by Petzinger et al. In the following section a brief discussion of the model will be presented followed by a description of a method involving Laplace transformed parameters due to A.T.Fiory that was used in fitting the data.

3.4.1 Multiple trap model for the transverse relaxation function

A general expression for the transverse relaxation function has been obtained by Petzinger et al. for a non-stationary distribution of diffusing particles by treating the interaction of μ^+ spin with the internal magnetic field of the solid using time dependent perturbation theory. Since the implanted muons in an impure solid start with non-equilibrium

spin and location, and since it takes time for the muon to relax to the equilibrium site occupation, the overall decay of the polarization is a function of the rate at which this relaxation takes place. The result for $G_x(t)$ in terms of correlation functions is given as:

$$G_x(t) = \exp - \left[\sum_i \Delta_i^2 \int_0^t dt' \int_0^{t'} dt'' F_i(t'') G_{ii}(t'-t'') \right] \quad (3.23)$$

$$\text{where } F_i(t'') = \sum_j Q_j G_{ij}(t'')$$

Here Q_j is the initial site distribution function for the ensemble of muons; $G_{ij}(t'')$ is the probability that a muon initially at site j will be at site i a time t'' later; $G_{ii}(t)$ is the autocorrelation function for a muon at site i ; and Δ_i^2 is the second moment of the static nuclear frequency distribution at site i . The sum runs over all interstitial sites in the crystal.

If Q_j is given its equilibrium value, eqn.(3.23) goes to the time independent Abragam form. But if Q_j does not represent statistical equilibrium, the rate of relaxation to equilibrium enters into the expression. We shall approximate $Q_j = 1/N$, although in the presence of impurities the assumption of uniform distribution may not be entirely justified.

Let us consider the case where the impurity concentration is relatively dilute and regroup the sum in the above equation into host sites characterised by a mean time of stay t_0 and trap sites ($m=1,2,\dots,M$) characterized by mean times of stay t_m , and trap concentration c_m . With our assumption of initially random muon distribution,

$$F_0(0) = 1 - c,$$

$$F_m(0) = c_m, \quad m \neq 0$$

The time dependent probabilities of the host and the trap occupancy are then given by the solutions to the rate equations:³⁸

$$dF_0/dt = (1-c) \delta(t) - c p_0 F_0 + \sum_m p_m F_m \quad (3.24)$$

$$dF_m/dt = c_m \delta(t) + c_m p_0 F_0 - p_m F_m, \quad m \neq 0$$

Here c is the total trap concentration $c = \sum_m c_m$, p_0 is the jump rate between two host sites. The detrapping rate p_m ($m > 0$) is given by: $p_m = p_0 \exp(-E_m/kT)$, where E_m is the binding energy of the trap site. The autocorrelation function for any site of type m is taken to be $G_m = \exp(-t/t_m)$. Due to the lack of a quantitative theoretical model, host jump

rate p_0 is parameterized by an empirical temperature dependence:

$$p_0 = a e^{-E/RT} + b + cT \quad (3.25)$$

In the Flynn-Stongher theory of diffusion, the terms could have the following significance: The Arrhenius behavior represent high temperature diffusion; at low temperature, the constant term is proportional to the coherent tunneling rate, and the linear term represents one phonon assisted tunneling that depends upon the strain broadening. The solution to the above equations can be obtained easily in terms of Laplace transforms. The method is described in the next section.

3.4.2 The Laplace Transform method

We can write the transverse relaxation function as:

$$G_x(t) = e^{-Y(t)} \quad (3.26)$$

and define a new parameter α :

$$\alpha = \int_0^{\infty} e^{-st} (dY/dt) dt \quad (3.27)$$

Alpha is the Laplace transform of dY/dt , with s having a specific value: $s^{-1} = t_{\mu} = 2.2\mu s$, the muon lifetime. Now from the preceding section,

$$Y = \sum_i \Delta_i^2 \int_0^t dt' \int_0^{t'} dt'' F_i(t'') G_{ii}(t'-t'') \quad (3.28)$$

$$dY/dt = \sum_i \Delta_i^2 \int_0^t dt' F_i(t') G_{ii}(t-t')$$

and

$$\alpha = \sum_i \frac{\Delta_i^2 \bar{F}_i(s)}{p_i + s}, \quad i = 0, \dots, N. \quad (3.29)$$

Taking the Laplace transform of the rate equations (3.24), we have a set of linear equations that can be solved numerically:

$$\bar{F}_0 - 1 + c = -p_0 c \bar{F}_0 + \sum_n p_n \bar{F}_n \quad (3.30)$$

$$\bar{F}_0 - c_n = p_0 c_n \bar{F}_0 - p_n \bar{F}_n, \quad n \neq 0$$

Experimental values for the α (alpha) parameter can be obtained from a Gaussian or an exponential fit, e.g., for the former case $\alpha = \Delta^2 t_c^2$. Thus the data can be fitted to these simpler equations to obtain the trap concentration, trap

binding energy and trapping rate for multiple traps, without doing the convolutions in Eqn.(3.23).

Chapter IV

EXPERIMENTAL DETAILS

4.1 THE MUON CHANNELS

The LAMPF stopped muon channel (SMC) layout is shown in figure 12³⁴. The production target for the beam line is a rotating wheel of pyrolytic graphite (density 1.73g/cm^3) of 6-cm thickness along the beam direction. The impinging proton beam of 729-MeV suffers an energy loss of 22 MeV. 77% of the beam survives and is captured by the transport system.

The channel-- a permanently assembled array of 23 quadrupole magnets and 4 bending magnets--transports the beam through a stainless steel vacuum chamber (3 m torr.). First six quadrupole magnets serve to collect pions with a momentum acceptance of $\pm 4\%$ and a solid angle of 60 msr. A production angle of 65° (laboratory) is used. This 7.7m

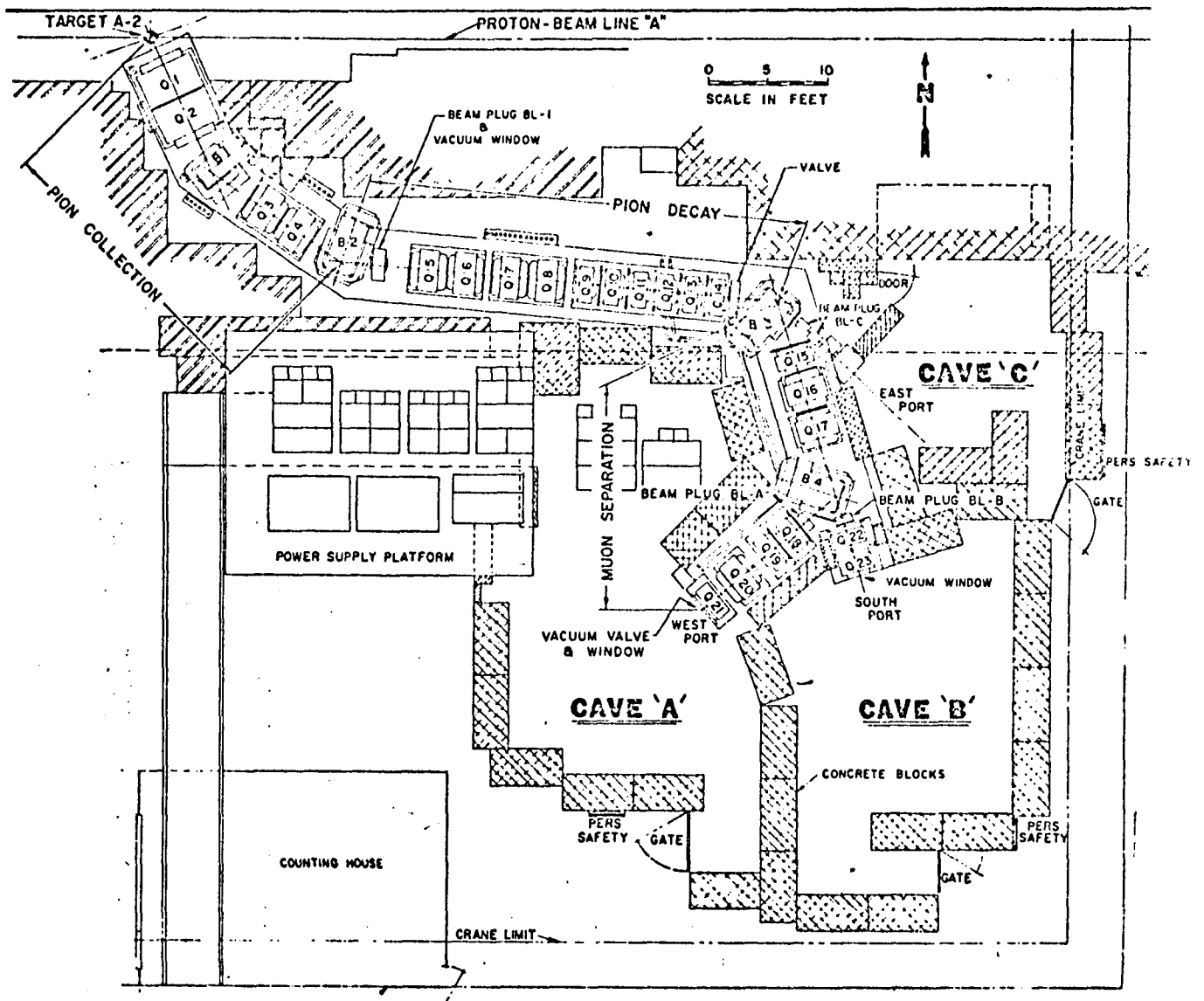


Figure 12: Layout of LAMP stopped muon channel

section terminates in a plug of 1T of U238, which shuts off the beam for access. The two bending magnets are used to momentum analyse the accepted particles and to eliminate neutrons. The pion decay section comprises the next 10 quadrupole magnets (radii 15 cm.) and is 11.2m long. It can capture muons upto $\pm 5^\circ$ (laboratory), accepting only extreme forward and backward decays. The remaining magnets separate the muon beam from pions and electrons and focus the beam onto the sample. For the backward decay beams used, a 20% transmission is typical. The beam is tuned by adjusting the magnets with an on-line PDP-11 program which can optimize 25 different parameters. SMC can produce muon beams upto 250 MeV/c with a peak stopping rate of $7.5 \times 10^4 \text{ u}^+ / (\text{uA.s.g/cm}^2)$. The muon beam used for our experiments had an incident momentum of 80 MeV/c with high muon spin polarization ($\geq 90\%$). A $\frac{7}{8}$ " diameter, 2" thick lead collimator was installed upstream of BM03 to get a small beam spot. A 5-mil Al window was installed at the end of the channel.

Fig.13 shows the meson channel of Space Radiation Effect Laboratories where the Al alloy experiments were performed in August, 1978. Its design and operation have been fully described elsewhere³⁵ This channel is now being installed at the alternating gradient synchrotron (AGS) at Brookhaven National Laboratory (BNL). We will give a very brief outline of the beam transport here.

The quadrupole doublet of lens A and B, each with its own power supply, was followed by a linear array of 24 identical quadrupole magnets, series fed from a single power supply. The channel accepted muons from pion decay within it, the magnets focussing alternately in the horizontal and the vertical plane. The upstream quad provided final vertical focussing;; the downstream quad provided the horizontal. The total distance from pion production to the sample was about 12 meters.

An internal carbon production target, impinged upon by approximately 600MeV protons, produced enough pions to generate muons at the rate of several thousands per second per square inch at the sample site.

4.2 THE SETUP

The setup for the Nb experiments was as follows: A hight adjustable table had been designed to house the magnet and the detectors. It slided on rails that could be bolted to the floor of the cave. The magnet could be oriented with its field direction along and perpendicular to the beam for longitudinal or transverse field experiments respectively. Before bringing the magnet table in, an Al shilding/collimator frame was attached to the field clamp and centered on

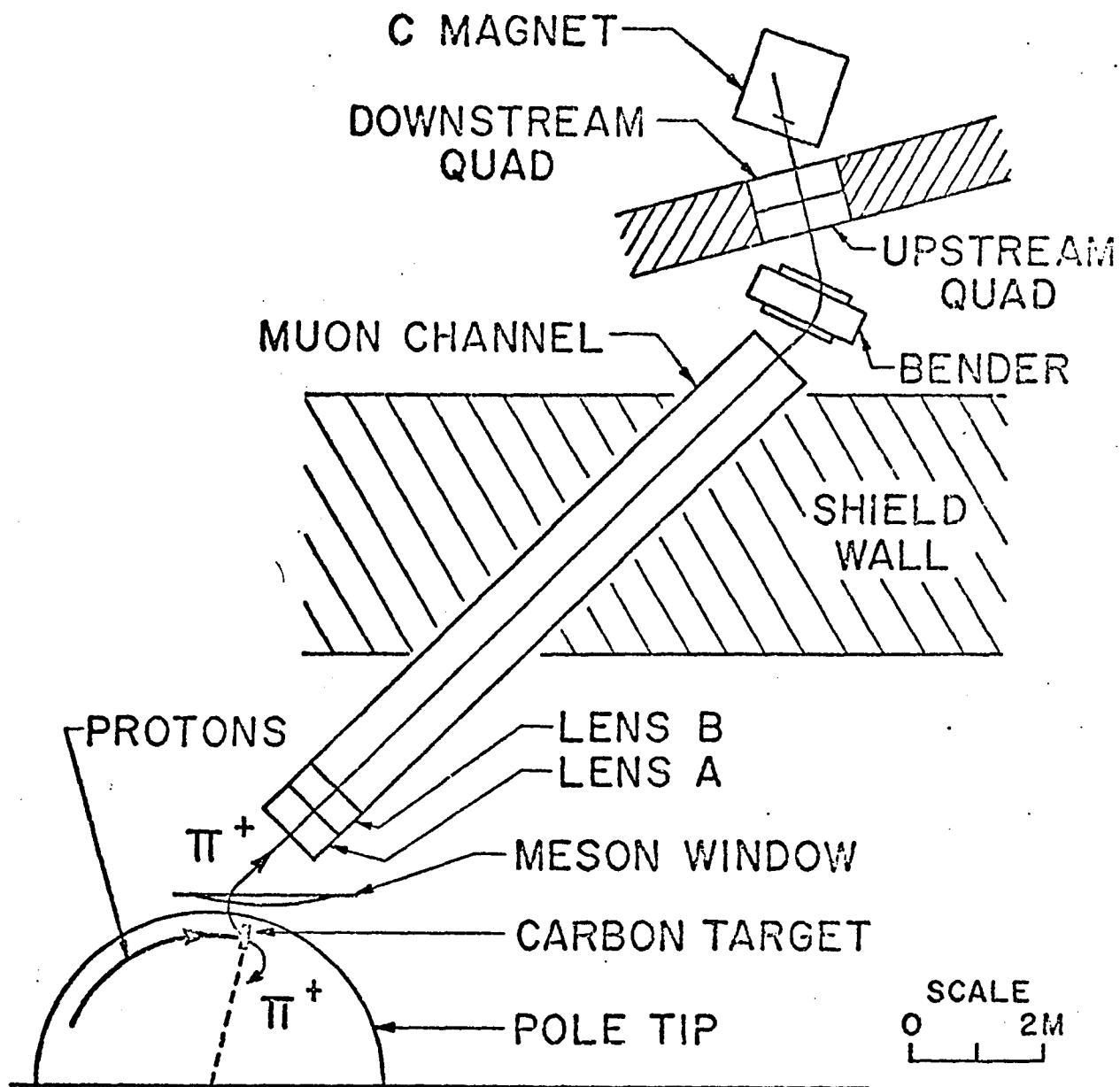


Figure 13: Layout of SREL meson channel

the beam. Lead bricks were stacked in the frame with a 4" x 4" hole centered on the beam line. All alignments had been attained meticulously with the aid of a laser. The rails were then bolted to the floor and the table oriented appropriately for the transverse or longitudinal case. For transverse measurements the counters and the collimators (C_2 and C_3) were arranged as in fig.14. Internal shielding was installed in the magnet and external shielding on the magnet table. Collimator sizes used are: $C_2=1.5"$, $C_3=1"$ for 100C operation ; $C_2=C_3=1"$ for the zero field case. Shielding was mounted on a separate table to protect the light pipes.

The initial runs in the transverse configuration showed large background contamination for time $t > 7\mu s$. The counter telescope was thereupon redesigned and the inner scintillators (E1's) were placed inside the vacuum jacket of the cryostat (Fig.15). This eliminated the muons stopped in the jacket from the histogram.

Also, for the longitudinal measurements (fig.15), collimator C_2 was connected to the beam line through a 13" copper shield pipe, centered on the beam. Crosswires were used on the faces of the magnet coils as a guide in alignment. Additional lead shielding was erected on top of the magnet to protect the BE and E2 light pipes.

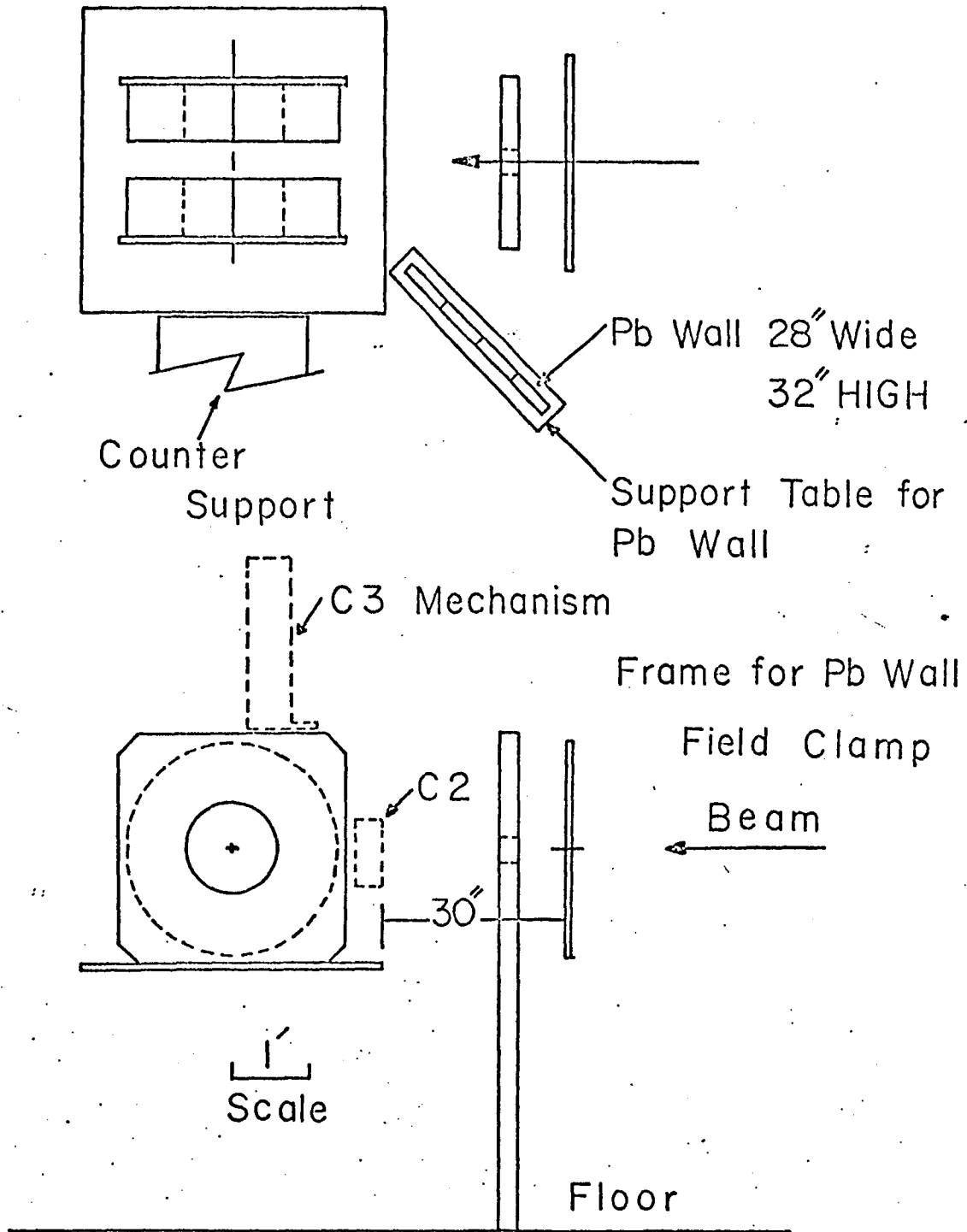
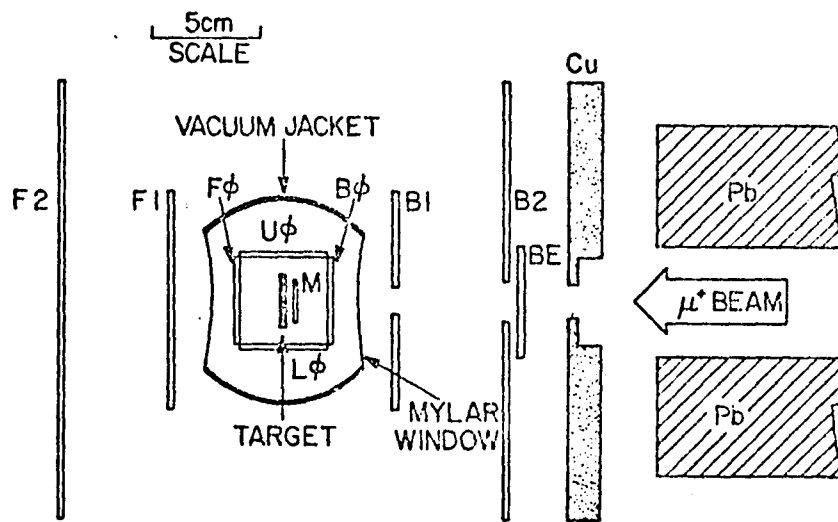


Figure 14: Transverse field setup



- EVENT DEFINITIONS:
- MUON STOP IN TARGET = $BE \cdot M \cdot \overline{F\phi} \cdot \overline{U\phi} \cdot \overline{L\phi}$
 - DECAY POSITRON (FORWARD) = $F\phi \cdot F1 \cdot F2 \cdot \overline{U\phi} \cdot \overline{L\phi} \cdot \overline{B\phi} \cdot \overline{BE}$
 - DECAY POSITRON (BACKWARD) = $B\phi \cdot BI \cdot B2 \cdot \overline{U\phi} \cdot \overline{L\phi} \cdot \overline{F\phi} \cdot \overline{BE}$

Figure 15: Longitudinal field setup

The transverse experiments with Al alloys used the following experimental setup: A large C magnet with 9" pole gap was used to produce the 500 G transverse field. Additional shims and trim coils were wrapped around the pole faces to attain uniformity of the field. A Hall probe was used to monitor the field inhomogeneity around the sample. The inhomogeneity was found to be about 25mG over the sample volume. A feedback system maintained the field uniform within 10mG.

The counter arrangement is shown in Fig.16. The positron telescope consisted of one annular detector with a 6.4 cm diameter hole (A) and a forward detector (F), both of 20cm X 20cm dimensions. The detectors used were plastic scintillators with standard photomultiplier amplification. Polyethylene degraders of appropriate thickness were used to maximize the muon stopping rate in the sample.

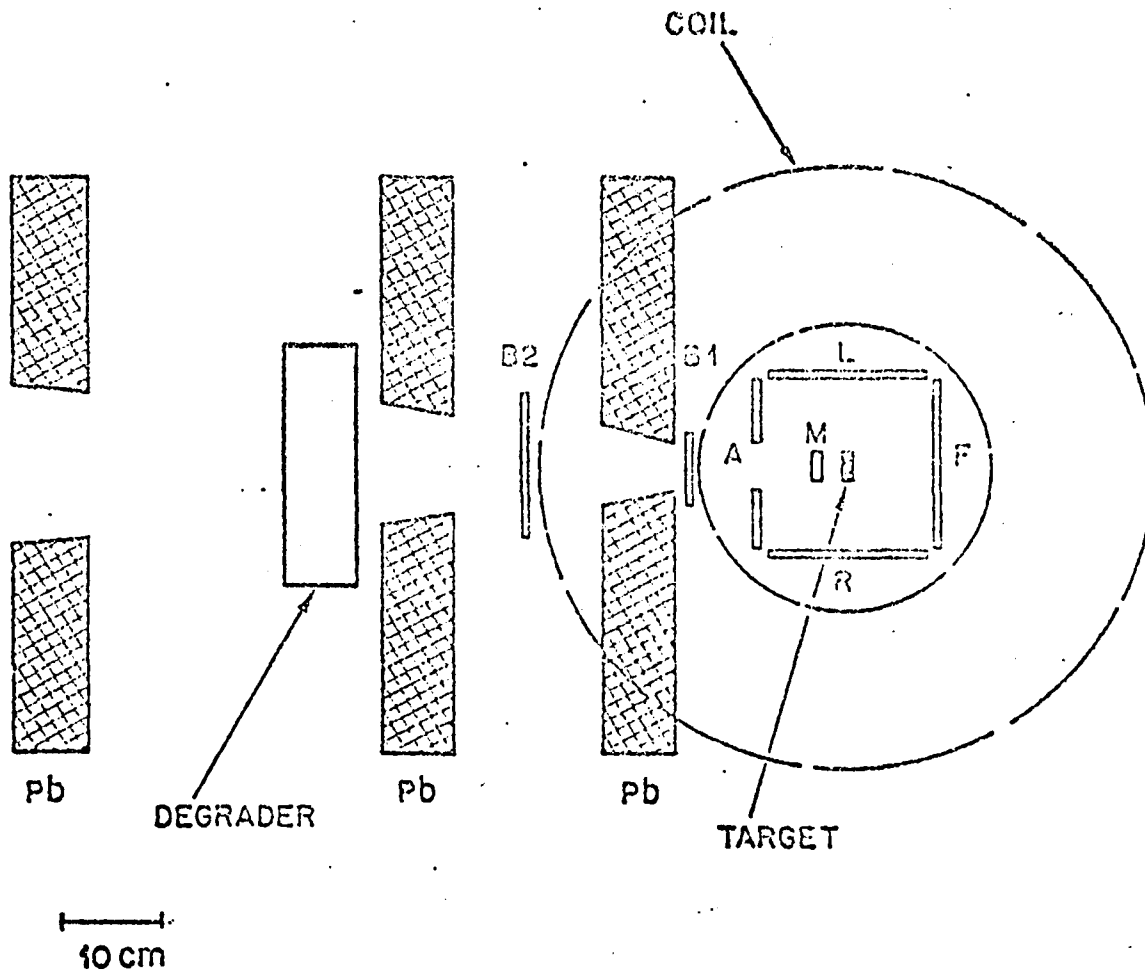


Figure 16: Transverse field setup at SREL

4.3 THE CRYOSTAT AND TEMPERATURE CONTROL

For the Nb experiments an Air-Product Heli-Tran Cryogenic system was used with a Cold-finger sample mount. Temperature was monitored using a carbon glass resistor (CGR), which along with the sample could be mounted on a pedestal with Al-foil and copper loaded grease. The pedestal fitted onto the cryotip. The CGR leads connect through a plug to those of a constant current source and a digital voltmeter. Temperature could be read directly from a calibration chart provided by the manufacturer. A heat shield was placed around the cryotip enclosing the sample and the CGR. Four $1\frac{1}{2}$ " x 2" counters were placed around this assembly for the longitudinal case to improve on the statistics. In the transverse arrangement the inner counters were placed outside the cryostat. A cylindrical stainless steel vacuum jacket with mylar windows surrounded the counters and could be secured with a strap.

Temperature was controlled by an Artronix temperature controller by sending heater current through a 100-watt ceramic resistor. A thermocouple (AuFe v. chromel) associated with the controller stabilized the temperature by controlling the feedback. Reference point for the thermocouple was maintained at 0°C using an ice point cell. Temperature sta-

bility within $\pm 0.1\text{K}$ could typically be attained with the controller. Operation of the system involved roughing the system to < 0.1 Torr and then pumping down to 10^{-4} Torr using the diffusion pump before inserting the transfer line. Liquid He dewar pressure was set at 250 mm for cooling down and then decreased to about 150 mm upon reaching operating temperature. To attain a given temperature point in the range of 10K to 100K, the thermocouple reading was monitored and the Artronix controller adjusted manually in steps. The CCR current source and the tip and the shield flow were set to proper range. Power input was manually adjusted to obtain correct voltage and stability. Then Artronix set point was readjusted to null the meter and a switch to the proportional mode was made. Table 3 lists the control parameter range used for the different temperature points.

The cryostat used for Al alloy studies was a standard commercial device not very different from the one described above. Seven to eight 3mm thick sample plates were stacked together in the cryostat. Carbon and Platinum resistance thermometers were used for temperature measurement. Temperature was controlled within 0.1K .

TABLE 3

Temperature control parameters for the Nb experiment

Temp	power set	gain	tip flow	shild flow
11 - 25 K	4.0 - 4.5	.5 - 1.0	max	max
25 - 50 K	4.5 - 5.5	1.0 - 3.0	30%	45%
50 - 80 K	5.0 - 5.5	3.0 - 6.0	25%	30%

constant current settings (CGR)

Temp	Current (ma)
5 < T < 13	10
13 < T < 100	100

4.4 THE SAMPLES

The Nb sample was a single crystal disk 2.5cm in diameter by 1.0cm thick spark cut parallel to the (110) plane from a cylindrical host crystal by H.K.Birnbaum and used at SIN and LAMPF in previous experiments^{37,18} It was given an oxygen annealing at 3×10^{-6} Torr and 2200°C to reduce the carbon impurities, and then outgassed at 4×10^{-10} Torr and 2300°C. Mass spectroscopic analysis reveals 200 ppm. substitutional Ta and less than 10 ppm. of other heavy substitutional impurities. Neutron activation studies on other crystals from the same parent crystal showed interstitial impurity concentration of C(100 ppm. at.) N(44 ppm. at.), and O(40 ppm. at.). Resistivity measurements implied smaller C and O concentration, however, indicating the possible existence of highly stable Nb-C-O complexes which may have precipitated along the grain boundaries. No hydrogen was found at the detection level of 50 ppm.at.

The doped Al samples were prepared at the Bell Laboratories as described below. 99.9% Al and appropriate amount of alloying elements (Mg, Si, Ag) were melted by rf induction heating in a MgO crucible and cast into 2 Kg ingots. These were then hot rolled to a thickness of 3mm, and cut into 10.2 cm x 7.6 cm rectangular pieces. The samples were heat

treated for 8 hours at 800-825K and quenched to 273K in brine. Cooling times between 0.05s and 0.2s were recorded. Samples were stored at temperatures below 200K to avoid thermal aging.

Mass spectroscopic analysis showed the samples to have 0.1% of Ag, Mg and Si respectively at a 5% level of accuracy. The Al(Si) samples were put through different heat treatments after the first set of data was collected. The samples were annealed at 800K for 8 hours, and then cooled in air. A time constant of 250s was typical. After collecting another set of data these air cooled samples were heat treated again as above, and cooled in the oven with the power off. Time constants of 4 hours were recorded for these oven cooled samples.

4.5 DATA ACQUISITION

A schematic diagram of the standard electronic logic used for the Nb experiments is shown in Fig.17. For our experiments only one pair of telescopes were used.

The transverse data were collected in a multiple TAC/ADC mode using normal time histograms (μ starts TAC, e^+ stops TAC). The longitudinal data were collected in a single TAC/ADC mode using inverted time histogram (e^+ starts TAC, μ stops TAC). This increased the efficiency of the TAC by eliminating the dead time associated with the muons which did not contribute to a good event. Time calibration was done by a pulse generator that put out stop signals at a fixed time interval from the random start pulse. The start pulse was routed to the D-input of the Mu. \bar{B} module. The stop signal was routed to the D-input of the F positron coincidence module.

After attaining temperature stability, zero field data were taken in both transverse and longitudinal configuration with field turned off. Then magnets were turned on for data with field. For each temperature point data were collected for about 4 hours, corresponding to approximately 1 million events. The data were analysed on-line with a PDP computer using eqn.(2.25). A fitting procedure for the static Kubo-

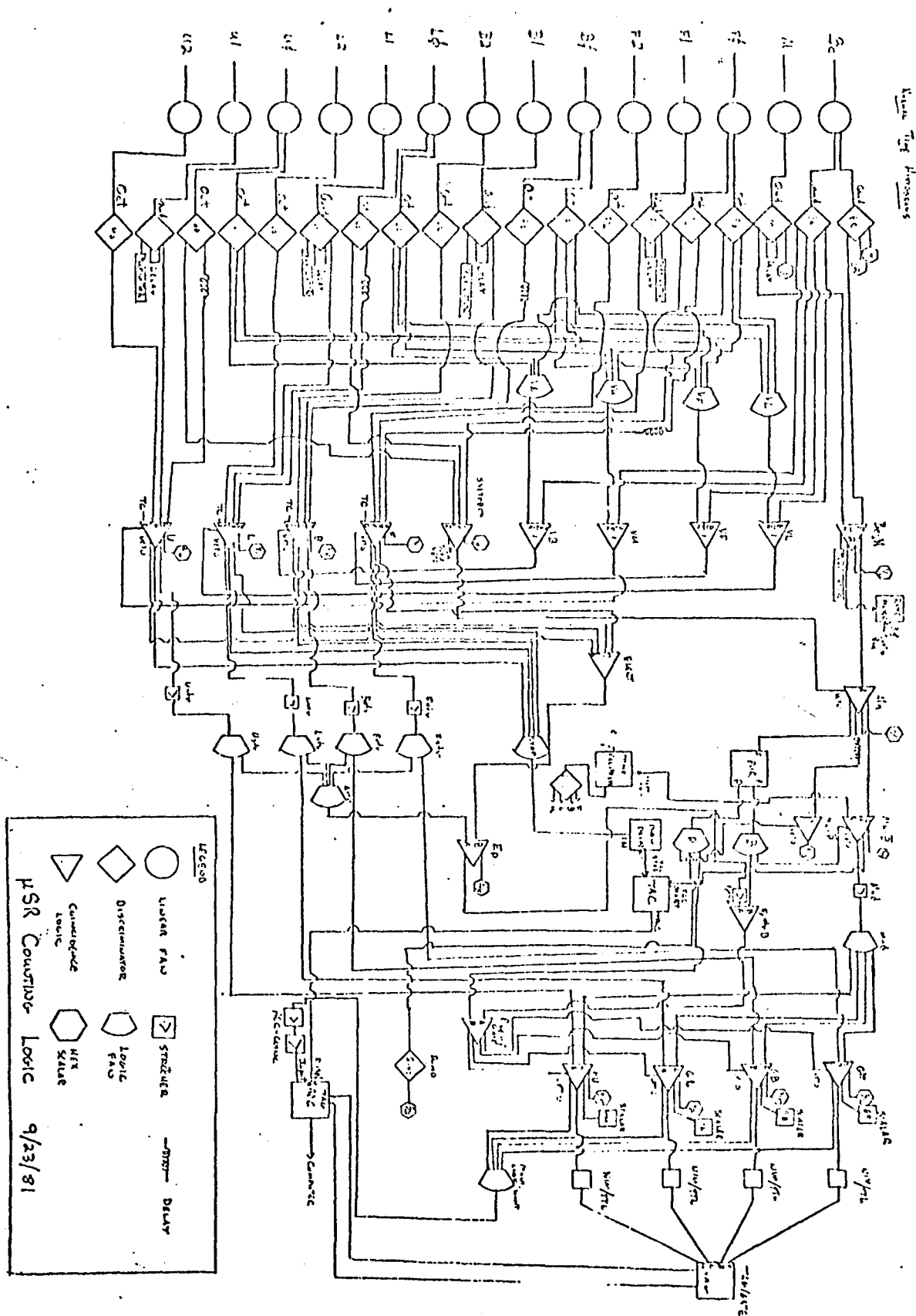


Figure 17: Electronic logic: LASL experiment

Toyabe case was available. The temperature was constantly monitored for stability. At 46K data point some fluctuation in the temperature took place in the longitudinal configuration. To fit such data. A Gaussian and an exponential form for the transverse relaxation were also available for fitting transverse data.

The electronic logic used at SREL is shown in Fig.18. TAC was started by a μ^+ , and stopped by an e^+ detector. A multichannel pulse height analyser (a Northern Scientific 710 with 1024 channels and a quadrant of a kicksort 711 with 4096 channels) collected the TAC output into histograms. Time calibration was done by starting the TAC with a time mark generator, and stopping it by a pulser.

Temperature points were selected initially at a regular interval. Data were taken for a little over an hour for each point, collecting over a million events.

The on line fitting to a Gaussian depolarisation rate was used. A finer mesh of temperature was selected whenever a variation was observed in the depolarisation rate.

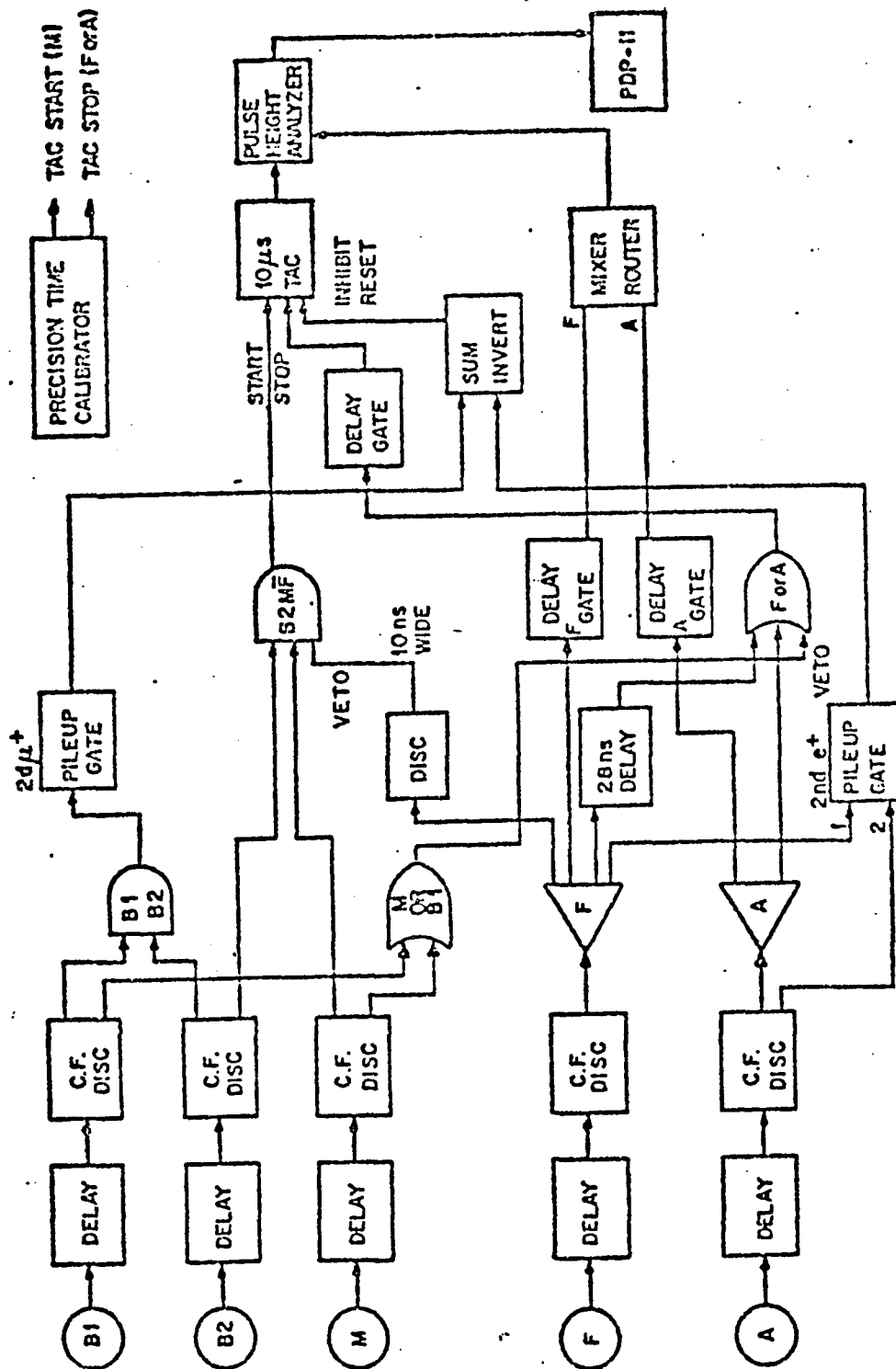


Figure 18: Electronic Logic: SKEL experiments

Chapter V

DATA ANALYSIS

The on line data analysis procedure has been discussed in the previous chapter under the data acquisition system. In this chapter we will be dealing with the detailed analysis carried out on the IBM 370 at the College of William and Mary. The CPU time and memory region requirements of the iterative non-linear least square fitting routines employing numerically computed extended precision functions demanded the resources of a large mainframe computer. The visual aid of a Tektronix terminal was especially useful during the early phase of fitting, in determining appropriate guess parameters. Data from PDP ASCII tapes were read and converted into EBCDIC format and stored in disk files.

5.1 ZERO AND LONGITUDINAL FIELD DATA IN NB

The 11K temperature point was used for obtaining the best values for the polarization asymmetries, the background ratios, and the ratio of the normalization constants, alpha, for the forward and the backward telescopes. Assuming the muon to be static at this point, we adopted the simple one parameter Kubo-Toyabe form for the relaxation function $G_z(t)$ in the fitting equations,

$$n_f(t) = n_f^0 \left[e^{-t/t_\mu} \{ 1 + a_f g_z(t) \} + b_f \right] \quad (5.1a)$$

$$n_b(t) = n_b^0 \left[e^{-t/t_\mu} \{ 1 - a_b g_z(t) \} + b_b \right] \quad (5.1b)$$

which were used simultaneously to fit the forward and the backward histograms respectively. In Eqns. (51):

n_f^0 and n_b^0 are the normalization factors for the forward and the backward histograms.

a_f and a_b are the polarization asymmetries for the forward and the backward telescopes.

b_f and b_b are the background ratios for the above telescopes.

$g_z(t)$ is given by (cf. Eqn. (3.5)):

$$g_z(t) = 1/3 + 2/3 \cdot (1 - \Delta^2 t^2) \exp(-\Delta^2 t^2 / 2) \quad (5.2)$$

where Δ is the gaussian width of the local fields.

The data were compressed with 90 channels per bin. An IBM IMSL routine for non-linear least squares fitting called ZXSSQ was adapted to minimize the chi-square of the fit. The fit for the above run has a chi-square of 1.01, shows a vanishing slope in $g_z(t)$ at $t=0$ and a recovery to $1/3$ at $t > 7\mu\text{s}$. Thus the five parameters a_f , a_b , b_f , b_b , and $\rho = n_f^0/n_b^0$ are very well determined from this run. These were used in the extraction of the relaxation function $G_z(t)$ from all the temperature points, including one other 11K data point taken at the end of the experiment.

To obtain the backgrounds for the histograms an estimate of the normalization constants (cf. eqns. 2.24) N_f^0 and N_b^0 was made from the early channels of the histograms where the data have the form:

$$N_f(t \rightarrow 0) = N_f^0 \left[e^{-t/t_\mu} (1 + a_f e^{-\Delta^2 t^2}) + b_f \right] \quad (5.3a)$$

$$N_b(t \rightarrow 0) = N_b^0 \left[e^{-t/t_\mu} (1 - a_b e^{-\Delta^2 t^2}) + b_b \right] \quad (5.3b)$$

The experimental relaxation function, $G_z^{\text{ex}}(t)$, is then computed as:

$$G_z^{\text{ex}}(t) = \frac{N'_f(t) - \alpha N'_b(t)}{a_b N'_f(t) + \alpha a_f N'_b(t)} \quad (5.4)$$

Here $N'_f(t) = N_f(t) - N_f^0 b_f$, $N'_b(t) = N_b(t) - N_b^0 b_b$, and the other parameters are as defined earlier. For the zero field data a display of this quantity already shows whether trapping or detrapping is taking place at a particular temperature point by the degree of recovery at $t \rightarrow \infty$. Appropriate functional forms from Chapter III were then employed to fit $C_z^{\text{ex}}(t)$, both at zero and 15 gauss fields, and values for Δ , and v or r were obtained. As a double check, histograms were also fitted directly to the accepted model permitting all the parameters to float. The values for the asymmetries, the background ratios, and the alpha parameter thus obtained were then checked against the 11K values for consistency. A list of these parameters is given in Table 4

TABLE 4

Variations in parameter values from run to run

Temp	Pa1	Pa2	Bgr1	Bgr2
11K	.244(4)	.211(4)	.0370(3)	.0406(3)
18.5K	.241(5)	.206(6)	.0392(6)	.0407(7)
24.3K	.237(5)	.213(5)	.0384(7)	.0406(6)
46K	.239(2)	.206(2)	.0333(3)	.0425(3)
77K	.244(4)	.211(4)	.0370(3)	.0406(3)

5.2 TRANSVERSE FIELD DATA

The forward and backward histograms of the transverse field Nb data were fitted simultaneously to the following functions (cf. Eqn.(2.22)):

$$N_1(t) = N_1^0 \left[e^{-t/\tau} \left\{ 1 + Pa_1 G_x(t) \cos(\omega t + \phi_1) \right\} + Bgr_1 \right] \quad (5.5a)$$

$$N_2(t) = N_2^0 \left[e^{-t/\tau} \left\{ 1 + Pa_2 G_x(t) \cos(\omega t + \phi_2) \right\} + Bgr_2 \right] \quad (5.5b)$$

In the static case of 11K,

$$G_x(t) = \exp(-\Delta^2 t^2 / 2)$$

is employed to obtain the best values of the parameters, Pa_1 , Pa_2 , ω , Bgr_1 , Bgr_2 , and Δ . For the other temperature points both the trapping and the detrapping models were tried out. For the trapping case, the function used for $G_x(t)$ was:

$$G_x(t) = \left[1 + \left\{ \frac{r}{\Delta \sqrt{2}} e^{r^2 / 2 \Delta^2} \left[\operatorname{erf}\left(\frac{\Delta t}{2} - \frac{r}{2\Delta}\right) + \operatorname{erf}\left(\frac{r}{2\Delta}\right) \right] \right\} \right] e^{-rt} \quad (5.6)$$

For the detrapping case, The Abragan formula:

$$G_x(t) = \exp\left(-\left[\frac{\Delta}{v}\right]^2 \cdot (e^{-t/v} - 1 + vt)\right) \quad (5.7)$$

was used for simplicity.

In case of the Al alloys, a Gaussian function was used to fit the histograms as in the static case of Nb. The parameter α (alpha) was then obtained by setting:

$$\alpha = \Delta t_{\mu}^2$$

The fitting equations (3.28-29) were then employed to obtain the least squares fittings to the data. The number of traps was varied with $M < 5$. The parameterization for the temperature dependence of p_0 was (Eqn. (3.25)):

$$p_0 = \exp(a-b/T) + d + eT \quad (5.8)$$

5.3 TIME CALIBRATION

The time calibration used to convert channels to time and vice versa is described below. As mentioned earlier the first set of Nb experiments in transverse geometry utilized two separate ADC's for the forward and the backward histograms, and so had to be calibrated separately for each telescope.

The histograms of calibration data consisted of peaks about the mean positions in the channels which correspond to integer multiples of t_{pulse} (=80 ns). These peaks often fall (a) entirely within one channel, but periodically (b)

split between two channels or more. Noting the periodicity of the evenly split peaks and using the vernier concept an estimate of the position of the peaks can be obtained to a fraction of a channel. In case (b) a second estimate (albeit exaggerated towards the channel with larger counts) is offered by the weighted mean of the channels. An estimate of the standard deviation may also be obtained to a fraction of a channel for the purpose of weighting the chi-square of a fit. The reduced data of pulse positions in fractional channels were then fitted to polynomials upto fourth order to see the improvements in accuracy with an increase in the order of the polynomials.

A quadratic fit was found sufficiently accurate for our purposes, and the coefficients in the equations,

$$i_n = at_n^2 + bt_n + c,$$

and
$$t_n = a'i_n^2 + b'i_n + c',$$

with $i_0=1$, $t_0=0$, obtained by a chi-square minimization procedure are displayed in the Table below.

TABLE 5

Calibration coefficients for time to channel conversion

Histogram	a	b	c
Both (Longit.)	$.37315 \times 10^{-6}$	2.526734	-2.49726
Forward	$.31761 \times 10^{-5}$	10.04319	-9.02319
Backward	$-.22949 \times 10^{-4}$	10.12763	-10.9963

5.4 THE FITTING ROUTINES

A versatile interactive Fortran program was developed to analyze the uSR data, both transverse and longitudinal, with the capability of reading histograms from tape or disk files, displaying them on a Tektronix terminal or a line printer, reducing the data into bins of specified size, and to fit the reduced data to any appropriate function using chi-square minimization via a non-linear least squares code. The program estimates normalization constants and zero time channel for the forward and backward histograms fairly accu-

rately. This is important in extracting relaxation functions from the two histograms. IMSL subroutine ZXSSQ in extended precision was used for fitting computed functions to the experimental data, allowing it to vary any desired number of parameters while keeping others fixed. ZXSSQ uses a modified Levenberg-Marquard algorithm employing finite differences instead of explicit differentiation. LEQTF subroutine, also a member of the IMSL package, was used for solving simultaneous linear equations. Numerical calculations of the finite field Kubo-Toyabe functions (Appendix A) generally took long CPU time and convergence through iterations was rather slow.

Chapter VI

RESULTS AND CONCLUSIONS

6.1 NB STUDIES

Our results for G_z^{ex} for zero and 15 Gauss longitudinal fields, along with the best fits of the appropriate models are shown in figs.19-27. These plots clearly demonstrate the mechanism of diffusion at the temperatures of interest, resolving the trapping-detrapping ambiguities mentioned in the introduction. At 11K (Figs.19-20 corresponding to point 1 of Fig.18) the data is completely consistent with the stationary (trapped) model: The recovery to one-third of the polarization is evident. The 18.5K plots (Fig.21-22, point 2) indicate detrapping with no sign of recovery of polarization at long times. The 24.3K plots (Figs.23-24, point 3), on the other hand, demonstrate significant recovery of polarization indicating that muons are finding traps. the

46K point is consistent with both trapping or stationary muons. The 77.3K plots (Figs.26-27, point 5) indicate eventual release from the traps. Thus even qualitatively the interpretation of monotonic increase of diffusion with temperature is seen to hold.

The solid curve in Fig.19 is the best fitted Kubo-Toyabe static model for zero field, while that in Fig.20 is the corresponding 15G static model (Eqn.3.8). In Figs.21, 22 and Figs. 26, 27 the solid lines represent the fitted detrapping model for zero and 15G field (Eqns.3.18) The fit in Figs.23 & 24 are the trapping models of Eqns.3.18, 3.22 corresponding to zero and 15G field respectively.

Table 6 summarizes the results.

Some typical transverse field data with appropriate fits are displayed in figs.28-32. Best fitted models for the different temperature points coincide with the conclusions from the longitudinal data. The parameters obtained from these fits are also displayed in Table 6

The errors in Table 6 are purely statistical. The agreement among the zero, longitudinal, and transverse fields is generally good; however the amount of scatter in the values, especially the trapping and the escape rates, indicates the probable presence of systematic errors in addition to statistical ones.

TABLE 6

Fitted parameters: Zero, ||, and \perp field Nb experiments

Region	T(K)	H(G)	Type of fit	v (us^{-1})	r (us^{-1})
		0		$.504 \pm .003$	
1	11.0	15	static	$.495 \pm .006$	
		100 \perp		$.493 \pm .010$	
		0		$.486 \pm .003$	$.647 \pm .016$
2	18.5	15	detrapping	$.477 \pm .005$	$.499 \pm .034$
		100 \perp		$.493 \pm .016$	$.607 \pm .085$
1 & 2 combined				$.495 \pm .002$	
		0		$.490 \pm .006$	$1.743 \pm .069$
3	23.5	15	trapping	$.453 \pm .006$	$2.23 \pm .21$
		100 \perp		$.490 \pm .022$	$1.10 \pm .15$
		0	trapping	$.504 \pm .005$	$3.26 \pm .08$
4		100 \perp		$.499 \pm .015$	$3.29 \pm .13$

Region	T(K)	H(G)	Type of fit	v (us^{-1})	r (us^{-1})
		0		$.473 \pm .003$	$.925 \pm .014$
5	77.3	15	detrapping	$.484 \pm .005$	$1.12 \pm .12$
		100 ⊥		$.529 \pm .008$	$1.11 \pm .05$
3, 4 & 5 combined				$.491 \pm .003$	

The Δ values of 11K and the 18.5K can be combined to obtain a value characterizing the low temperature trap: $\Delta_{LT} = .495 \pm .002 \text{ us}^{-1}$. Similarly, combining the Δ values of 24.3K, 46K and 77.3K a high temperature trap parameter emerges: $\Delta_{HT} = .491 \pm .003 \text{ us}^{-1}$. The values of Δ obtained from our analysis is compared with those reported earlier in Table 7.

We have found the Δ values for the zero, longitudinal, and transverse case to be same as expected. It may be pointed out in this connection that if nuclear moments were free to precess around the external field, then the effective Δ is reduced by a factor of $2/5^{21}$

$$\Delta_{\perp} = \frac{\sqrt{2}}{5} \Delta_0$$

In our case the interaction of the quadrupole moments of the Nb nuclei with the electric field gradients produced by the muons is much stronger than the Zeeman interaction ($H \ll 1 \text{ kG}$). Thus the niobium nuclei precess rapidly around the radial electric field gradient directions, so that the same time average of the nuclear magnetic field is seen in different field direction. The above argument holds exactly for polycrystalline samples, but for single crystals in low fields anisotropy is known to be very small⁴¹ and an approx-

TABLE 7

Comparison with earlier work

	$\Delta_{L,T}(\mu s^{-1})$	$\Delta_{HT}(\mu s^{-1})$
Our result	$.495 \pm .002$	$.433 \pm .033$
Ref. 19	$.454 \pm .011$	$.366 \pm .013$

The values from Ref. 19 have been multiplied by $\sqrt{2}$ to conform with our conversion.

imate equality of the zero and transverse field Δ 's should hold.

6.2 AL ALLOYS

The temperature dependence of σ (alpha) for Al(Ag), Al(Si) and Al(Mg) alloys are displayed in Figs. 33-37. For comparison one may note that the theoretical value for σ on the basis of the dipolar field contributions alone is 0.44 for a muon in an octahedral site and 0.12 for one in a substitutional site.

The Al(Si) data has a very complex structure, with peaks at 2K, 10K, 40K, and 120K. These peaks bear some resemblance to the Al(Cu) features³⁹ observed by Kossler et al. A five trap fit is obtained for this data over 4K-110K range.

Al(Ag) and Al(Mg) have slightly different character, and have fewer number of peaks over the same temperature range. A 3 trap fit was used for the Al(Ag) data, and a 4 trap fit for the Al(Mg).

The fits for Al(Ag), Al(Mg) and Al(Si) are shown in Figs. 33-35. Qualitatively the model shows a reasonable fit to the data. The uniqueness of the fits and the significance of the quantitative results are still uncertain. Table 8 displays the parameters obtained from the fits.

TABLE 8

Impurity conc., binding energy, and Δ for Al-alloys

Sample	m	$\Delta_m (\mu s^{-1})$	c_m (ppm)	E_m (meV)
Al(Si)	1	.227	2550	8.6
	2	.412	251	13.1
	3	.117	313	195
	4	.300	59.3	22.5
	5	.410	18.6	727
Al(Ag)	1	.215	879	21.2
	2	.235	121	58.6
	3	.410	37	710
Al(Mg)	1	.213	3200	22.6
	2	.129	1834	86
	3	.408	1460	37.0
	4	.410	19	2670

The overall picture of muons reaching high concentration low binding energy traps at lower temperature and lower concentration but deeper traps at higher temperature is borne out. The qualitative agreement with the Al(Cu) experiment is noteworthy. The fitted concentration of traps for the low temperature peak is about twice the nominal concentration of single impurities of Si. In case of Mg we find several peaks with concentration 1.5 to three times the actual concentration. Some of these values are artifacts of the fitting procedure as demonstrated by arbitrary kinks in the fitted curve. Prominent peaks can be identified however by inspection, and their concentration and binding energy inferred. The highest concentration, shallower traps most probably represent single impurity traps. Subsequent peaks with lower concentration but higher binding energy may be evidence of impurity clustering. We also note no appreciable difference in the data from various heat treatment. These preliminary studies indicate the need for a systematic exploration of the effects of the impurities in different concentrations and through various history of sample preparation. A more explicit theoretical model would make quantitative understanding of the influence of defect approachable. Zero field studies may be combined with the transverse field uSR to extract more information as in the case of Nb.

Appendix A

INVERSION OF LAPLACE TRANSFORMATION USING FOURIER SERIES

Let $F(s)$ be the Laplace Transform of $G(t)$:

$$F(s) = \int_0^{\infty} e^{-st} G(t) dt, \quad (\text{A.1})$$

where

1. $F(s)$ exists for $\text{Re } s > 0$, a condition that can always be satisfied by replacing $F(s)$ by $F(s+a)$, or equivalently by changing $f(t)$ to $f(t) \cdot \exp(-at)$, and
2. $G(t) = 0$, for $t=0$, which can be achieved by taking $G(t) - G(0)$ instead of $G(t)$, or equivalently by replacing $F(s)$ by $F(s) - G(0)/s$.

Using the transformation:

$$e^{-pt} = \cos \theta ,$$

where p is an arbitrary positive number, one has

$$G(t) = G\left(-\frac{\ln \cos \theta}{p}\right) = g(\theta)$$

$$\text{and } pF(s) = \int_0^{\pi/2} (\cos \theta)^{s/p-1} \sin \theta g(\theta) d\theta \quad (\text{A-2})$$

If we expand $g(\theta)$ in a Fourier Series:

$$g(\theta) = \sum_v C_v \sin(2v+1)\theta, \quad (\text{A-3})$$

The coefficients can be calculated, if the functional form of $F(s)$ is known, from the relation:

$$C_v = \frac{4}{\pi} \int_0^{\pi/2} g(\theta) \sin(2v+1)\theta d\theta. \quad (\text{A-4})$$

To express C_v in terms of $F(s)$, put $s=(2n+1)p$, $n=0,1,2,\dots$, in eqn. (A-2):

$$\begin{aligned} pF(\{2n+1\}p) &= \int_0^{\pi/2} \cos^{2n} \theta \sin \theta g(\theta) d\theta \\ &= 2^{-2n} \sum_{k=0}^n \left[\binom{2n}{k} - \binom{2n}{k-1} \right] \sum_{v=0}^{\infty} C_v \int_0^{\pi/2} \sin\{2(n-k)+1\}\theta \cdot \sin(2v+1)\theta d\theta \\ &= 2^{-2n} \frac{\pi}{4} \sum_{k=0}^n \left[\binom{2n}{k} - \binom{2n}{k-1} \right] C_{n-k} \end{aligned}$$

$$\sum_{k=0}^n \frac{2k+1}{2n+1} \binom{2n+1}{n-k} C_k = \frac{4^{n+1}}{\mathcal{J}} \text{pF}(\{2n+1\}p) \quad (\text{A.5})$$

Putting $n=0, 1, \dots$ in this equation we can compute C_v when the functional form of $F(s)$ or $sF(s)$ is known; p is chosen appropriately for the time range for which $G(t)$ is to be calculated-- large for small t , and vice versa. Table 9 gives the coefficients of C_v in the system (A-5).

This procedure was followed in computing Kubo-Toyabe model for the longitudinal field relaxation function. Convergence was obtained with 10 terms in the series.

TABLE 9

Coeffs. of C_v for computing inverse Laplace transforms

n	C_0	C_1	C_2	C_3	C_4	C_5	C_6	C_7
0	1							
1	1	1						
2	2	3	1					
3	5	9	5	1				
4	14	28	20	7	1			
5	42	90	75	35	9	1		
6	132	297	275	154	54	11		
7	429	1001	1001	637	273	77	77	1

REFERENCES

1. Gurevich, I.I., et al., Physics Letters, 40A, 143(1972)
2. Anderson, P.W., Physical Review, 109, 1492(1958)
3. Petzinger, K.G., Phys. Lett., 75A, 225(1980)
4. Petzinger, K.G., et al., Hyp. Int. 6, 223(1979)
5. A.T. Fiory, Hyperfine interaction, 6, 261(1979)
5. Brandt, W., Positron Annihilation, ed. Stewart, A.T., and Roellig, L.O., (Academic Press, New York, London 1967)
6. Abragam, A. Principles of Nuclear Magnetism, (Oxford, London, 1961)

7. Proc. First Int. Top. Meeting on Muon Spin Rotation (Rorsch 1978), ed. F.N.Gygax, W.Kundig, and P.F.Meier (North Holland Publ. Comp., Amsterdam 1979)
8. Proc. Sec. Int. Top. Meeting on Muon Spin Resonance (Vancouver1980) ed. J.H.Brewer and P.W.Percival (North Holland Publ. Comp., Amsterdam 1981)
9. Brewer, J.H., Crow, K.M., Gygax, F.N., Schench, A. 'Positive muon and muonium in matter', in Muon Physics, Vol. III, ed. Hughes, V.W. and Wu, C.S., pp.3-139, (New York, Academic Press, 1975)
10. Brewer, J.H., and Crowe, K.M., 'Advances in muon spin rotation' Ann. Rev. Nucl. Part. Sci., 28, 139-326(1978)
11. Seeger, A., 'Positive muons as light isotope of hydrogen', in Topics in Applied Physics, Vol. 28, Hydrogen in Metal-I, ed. Alefeld, G. and Volkl, J. (Springer-Verlag, Berlin-Heidelberg-New York 1978), pp. 349-397.

12. Schenck, A., 'On the application of polarized positive muons in solid state physics', in Nuclear and Particle Physics at Intermediate Energies, ed Warren. J.B., (Plenum, New York 1976), pp. 159-297.
13. Denison, A., Graf, H., Kundig, W. and Meier, P.F., 'Positive muons as probes in ferromagnetic metals', Helvetica Physica Acta, 52, (1979)460-517.
14. Seeger, A. 'Positive muons as probes for defects in crystals' Hyperfine Interaction, 6, (1979), 313-321.
15. Doyama, M. Progress in the study of point defects, ed. Doyama, M., and Yoshida, (University of Tokyo Press, Tokyo 1977)
16. Hyperfine Interaction, 8, 687(1979).
17. Weissenberg, A.O., Muons (North-Holland, Amsterdam, 1967)
18. Borghini, M., et al., Phys. Rev. Lett., 40, 1723(1978)
19. Birnbaum, H.K., et al., Phys. Rev., B17, 4143(1978)

20. Grebinnik, V.G., et al., Pisma Zh. Eksp. Teor. Fiz., 25, 322(1972)
21. Kubo, R. and Toyabe, T., in Magnetic Resonance and Relaxation, edited by R. Blinc (North-Holland, Amsterdam, 1967)
22. Yamazaki, T., Hyp. Int. 6, 115(1979)
23. Hyano, S., et al., Phys. Rev. Lett. 41, 1743(1978)
24. Hyano, R.S., et al., Phys. Rev. B20 850(1979)
25. Petzinger, K.G., Phys. Lett. 75A, 225(1980)
26. Boekema, et al., submitted to Physical Review B.
27. Segre, E., in Nuclei and particles, (W.A. Benjamin, New York, Amsterdam 1964)
28. V.G. Grebinnik, et al., JETP Lett. 22, 16(1975)
29. Grebinnik, V.G., et al., Soviet Physics J.E.T.P. 41, 777(1976)

30. Yamazaki, et al., Physica Scripta, 11, 133(1975)
31. Gorelkin, V.N., Smilga, V.P., Soviet Physics J.E.T.P. 42, 482(1976)
33. McMullen, T. and Zaremba, E., Physical Review B, 18, 3026(1978).
34. Thompson, P.A., et al., The stopped muon channel at LAMPF, Nuclear Instrumentation and methods, 161, 391(1979)
35. Funsten, H.O., Nuclear Instruments and Methods, 94, 443(1971)
36. Flynn and Stoneham Physical Review B 1, 3966(1970).
37. Brown, J.A., et al., Hyperfine Interaction, 6, 233(1979)
38. Petzinger, K.G., et al., Hyperfine Interaction, 6, 223(1979)
39. Kossler, W.J., et al., Physical Review Letters, 41, 1558(1978)

40. Peter Mayer, private communication.
41. Schilling, H. et al., *Hyperfine Interaction*, 8,
675(1981).

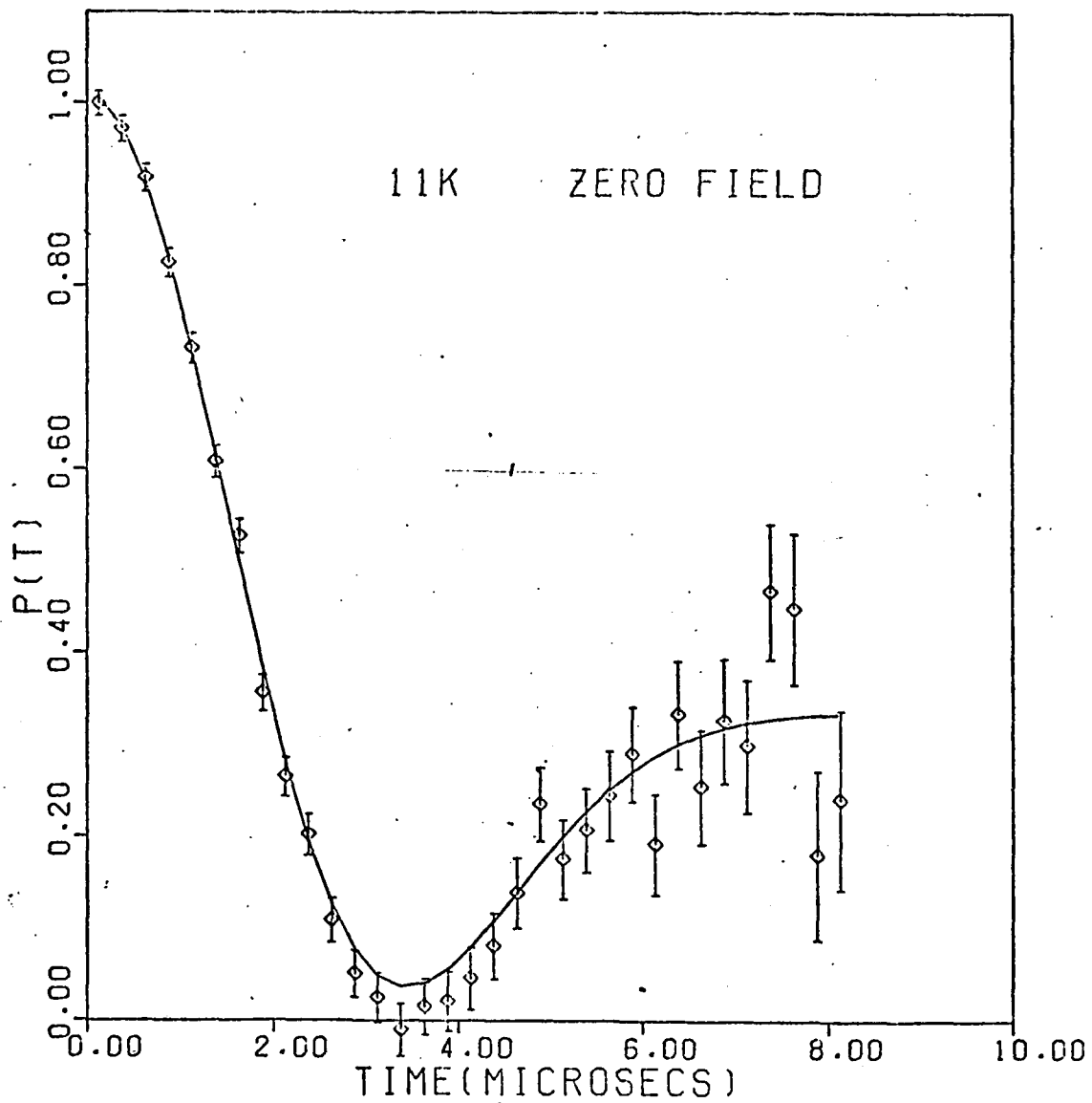


Fig. 19

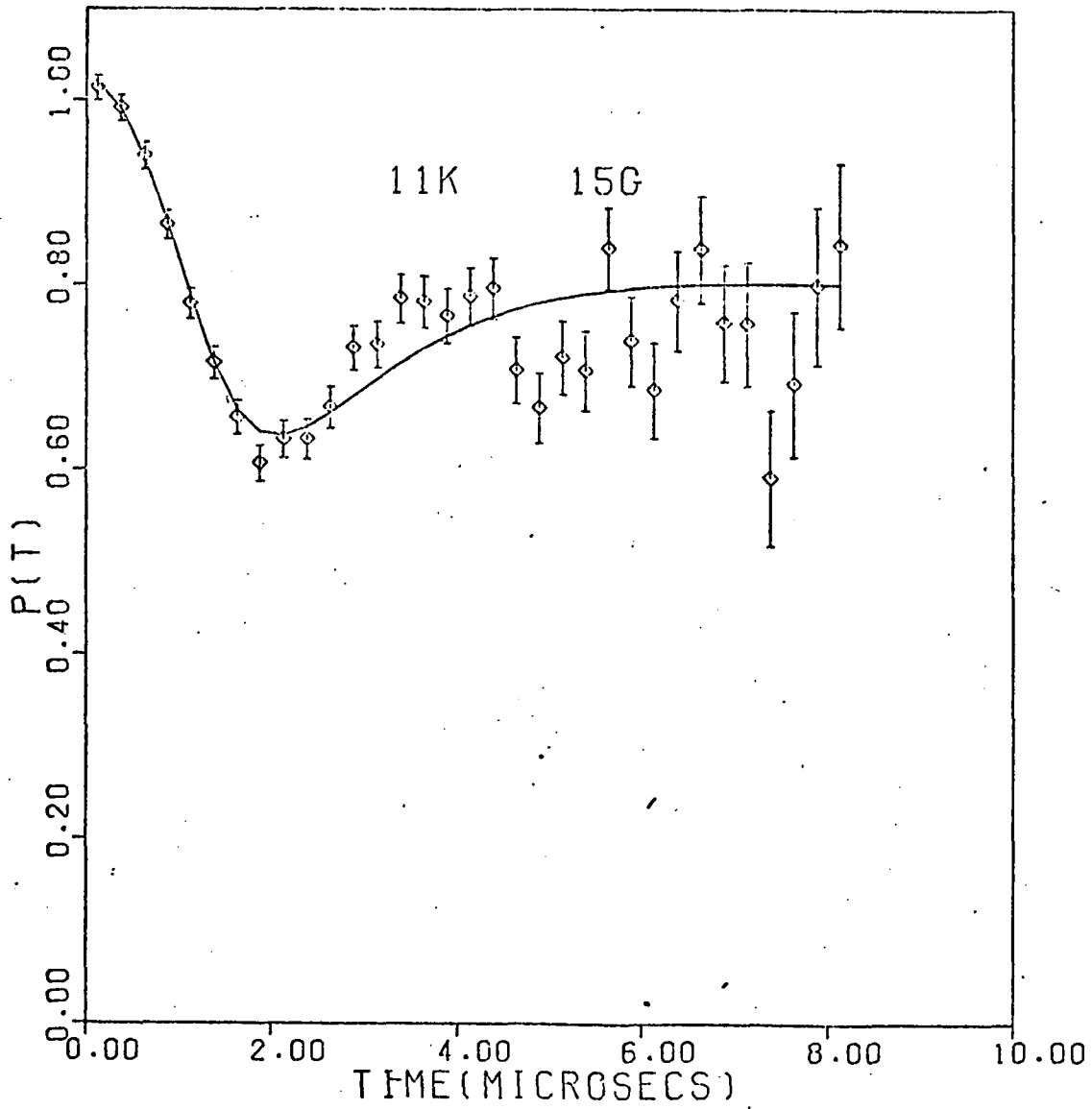


Fig. 20

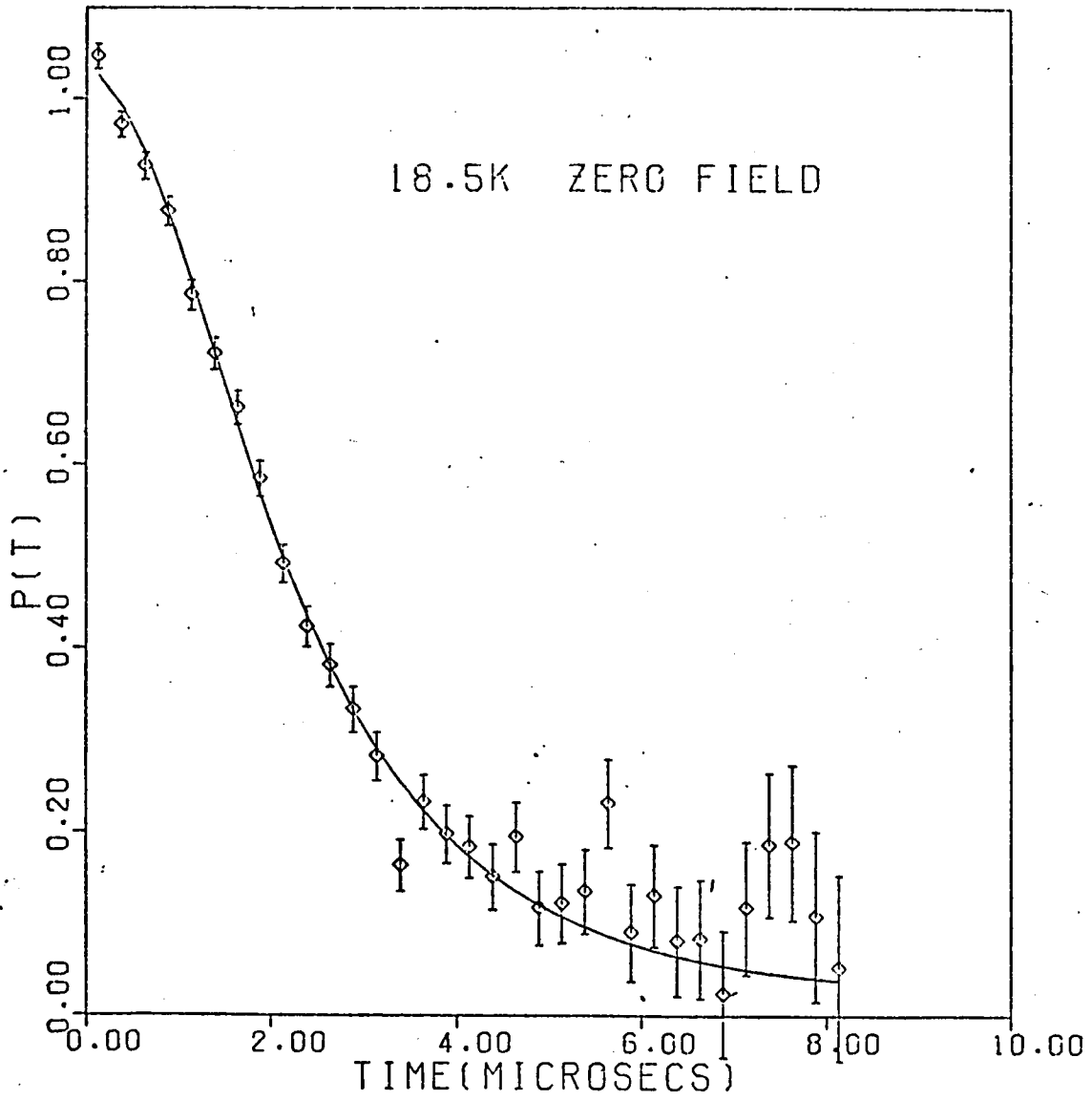


Fig. 22

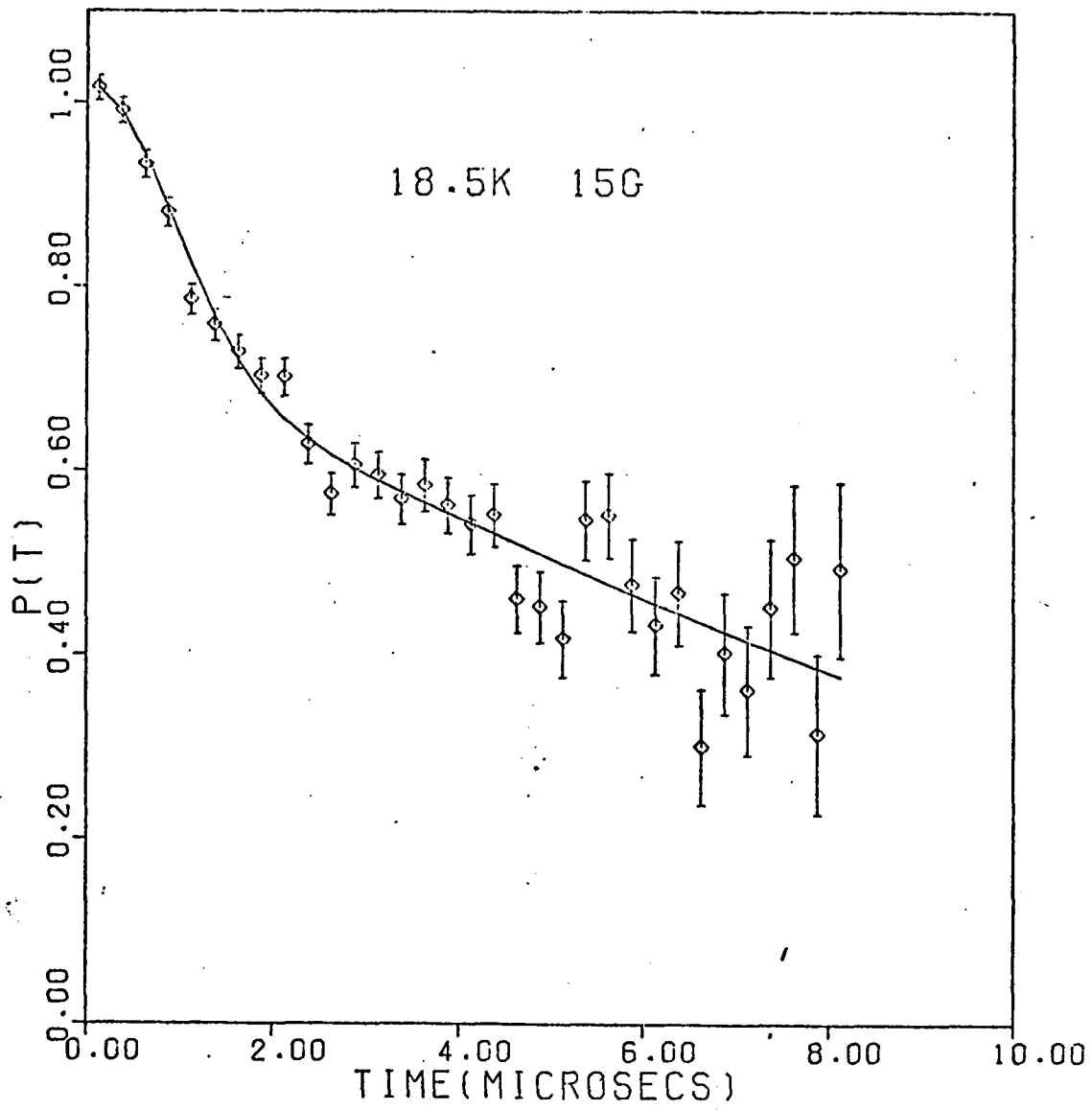


Fig. 21

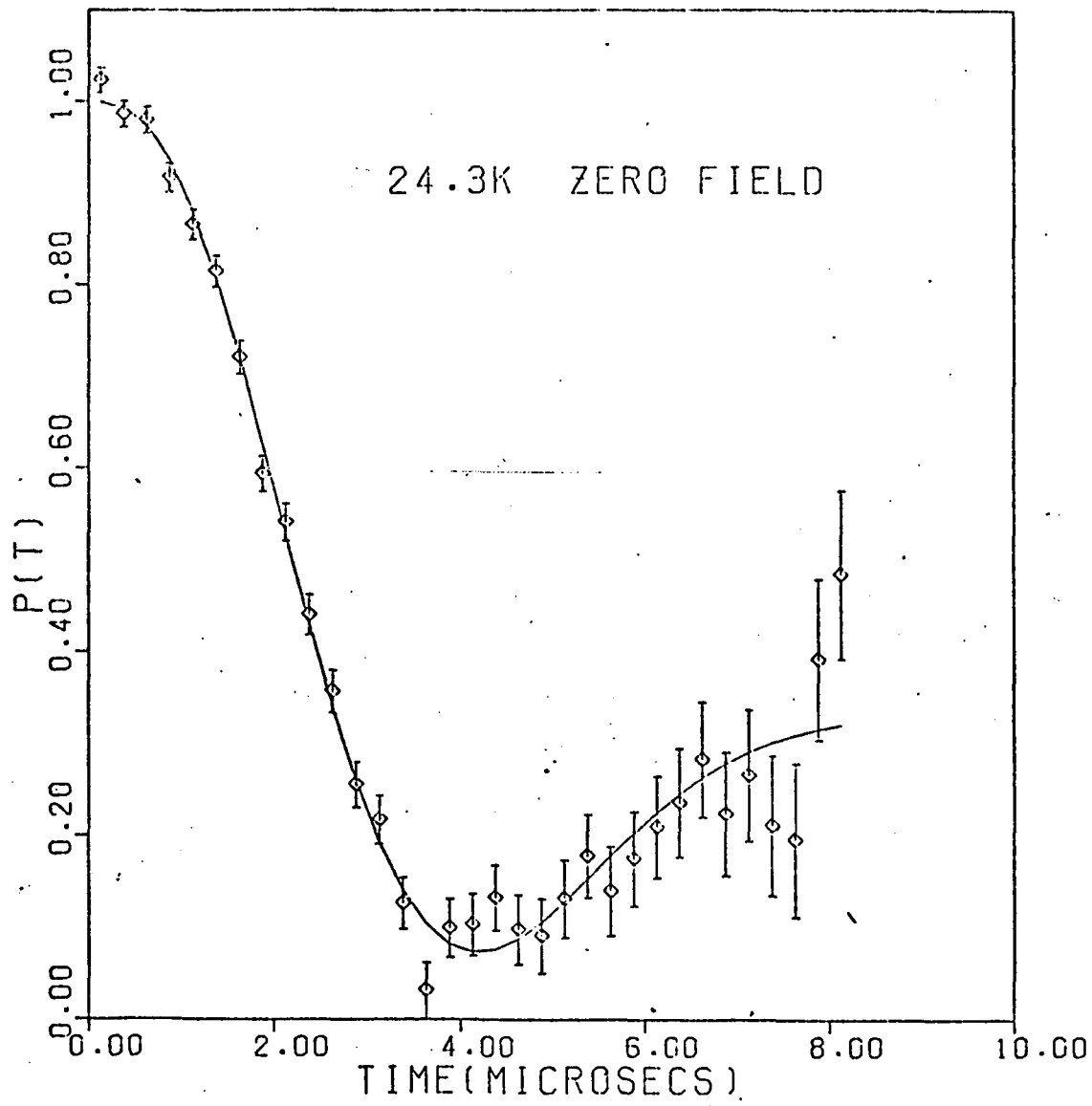


Fig. 23

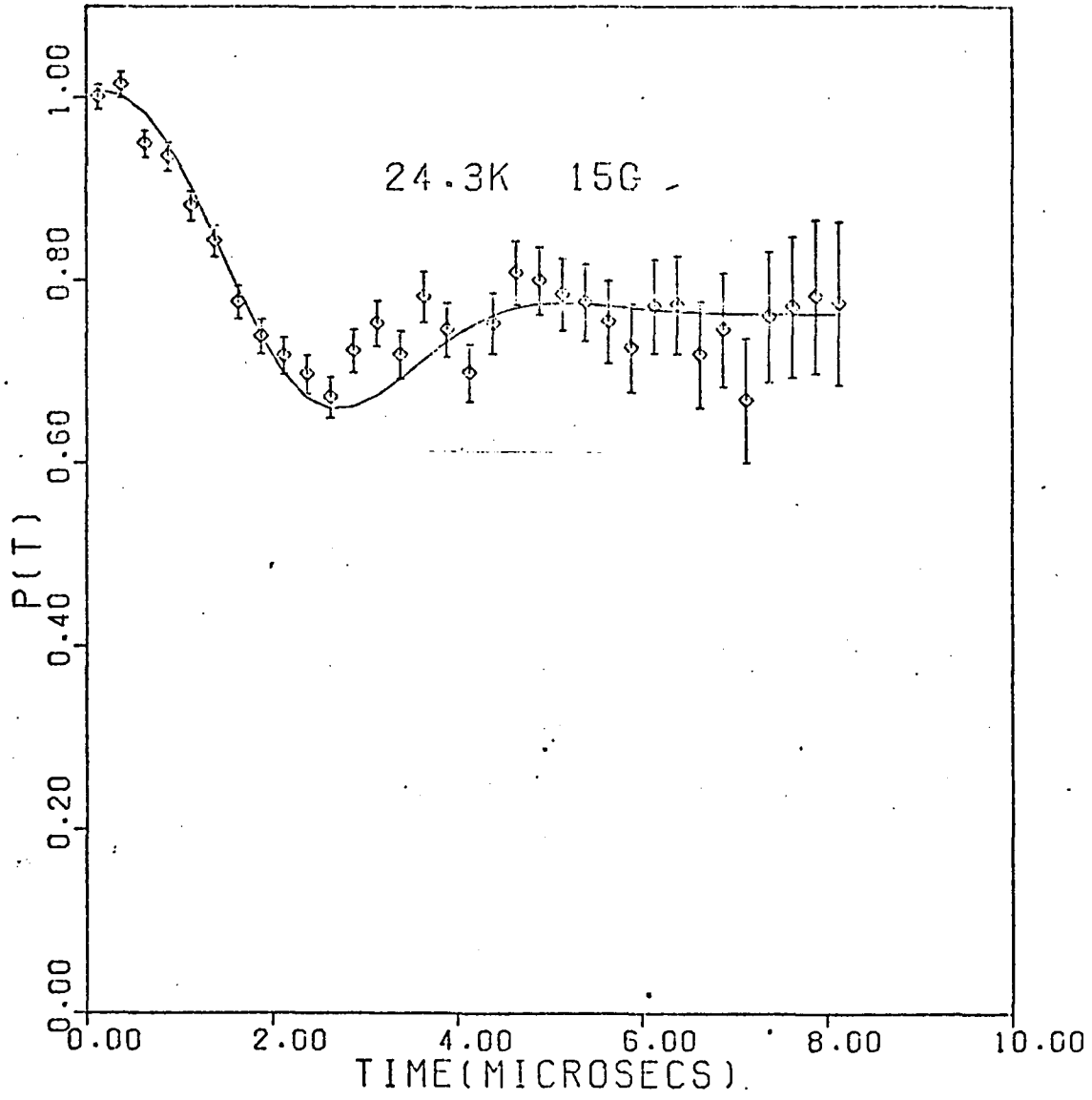


Fig. 24

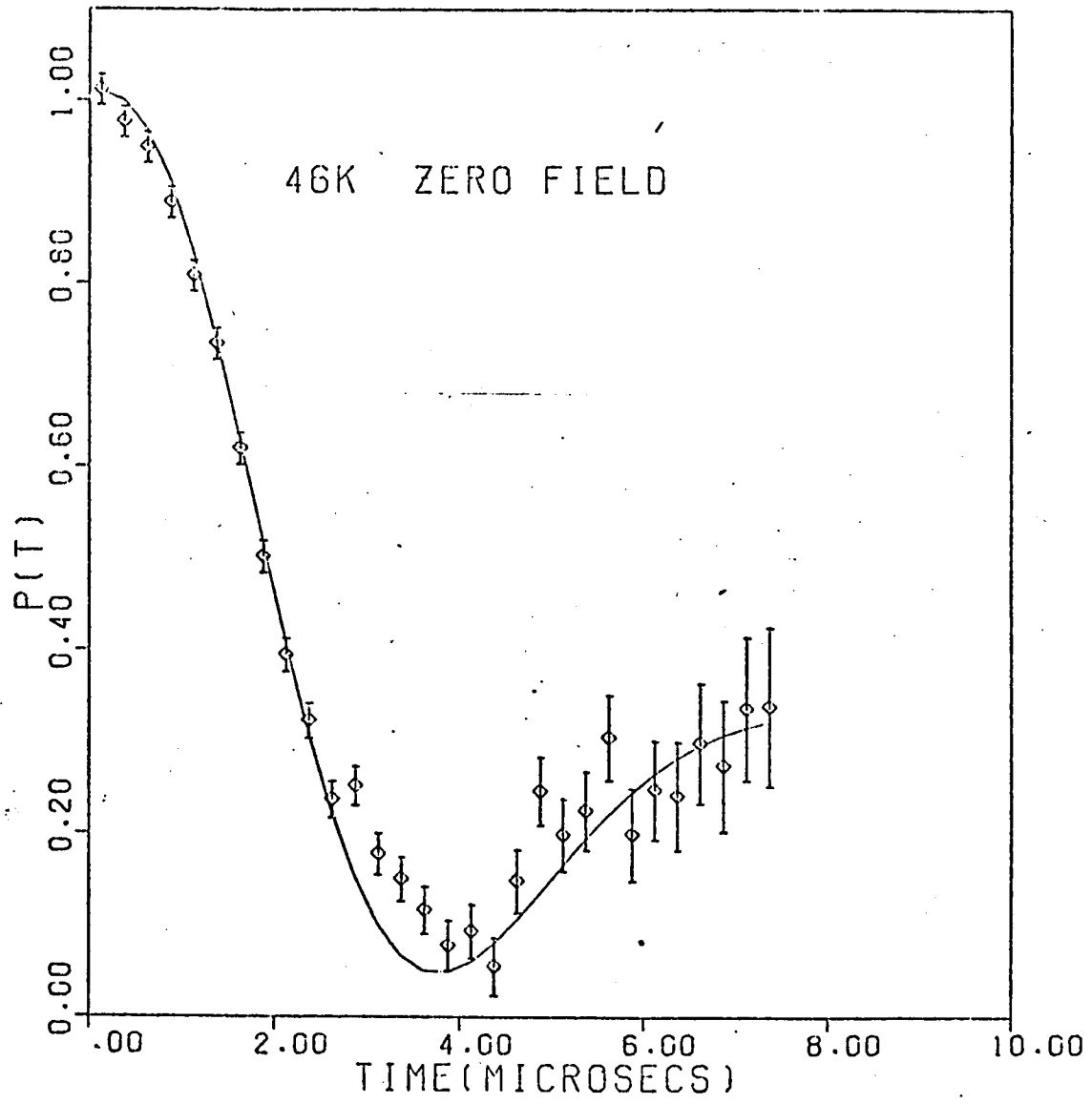


Fig. 25

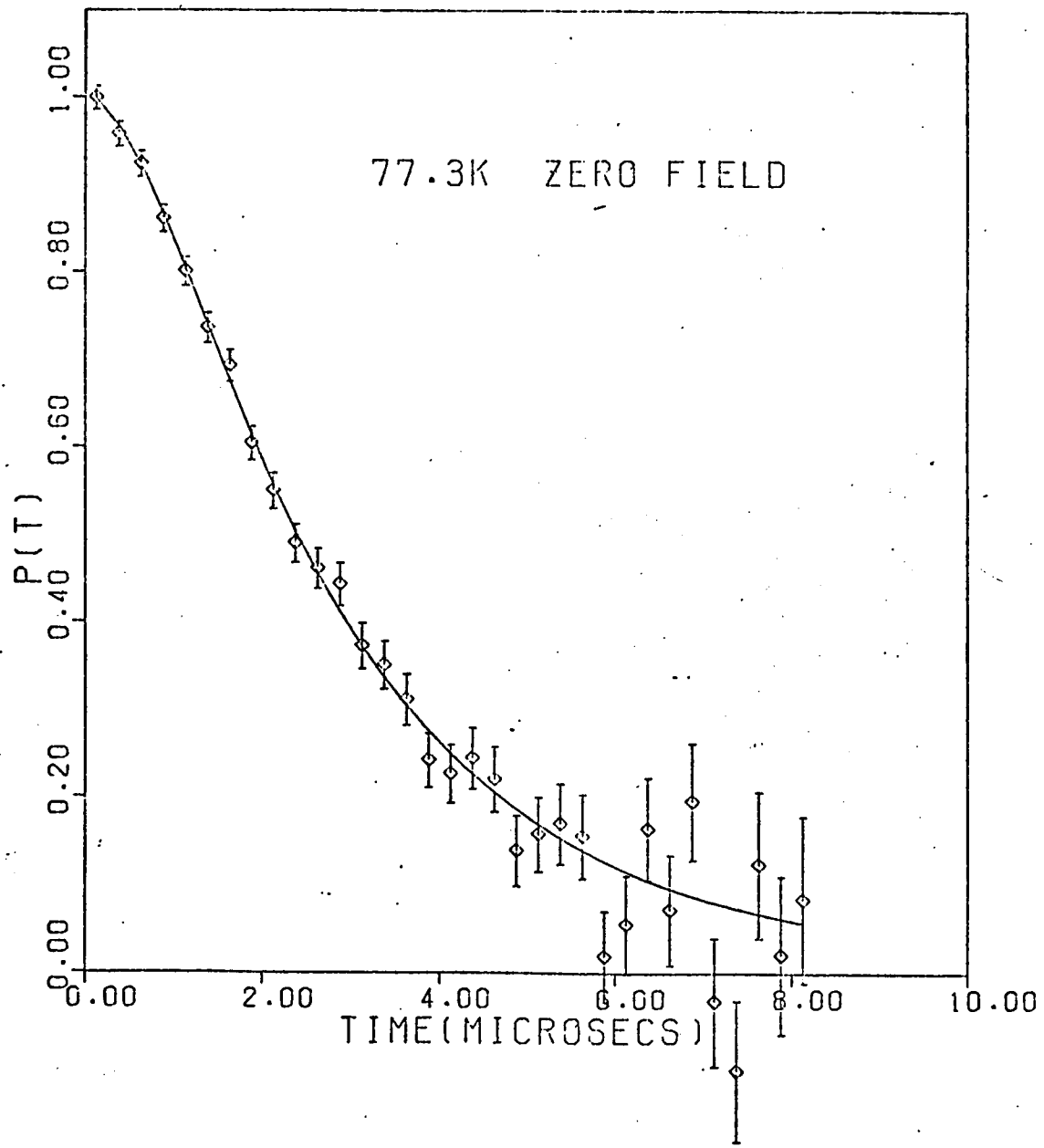


Fig. 26

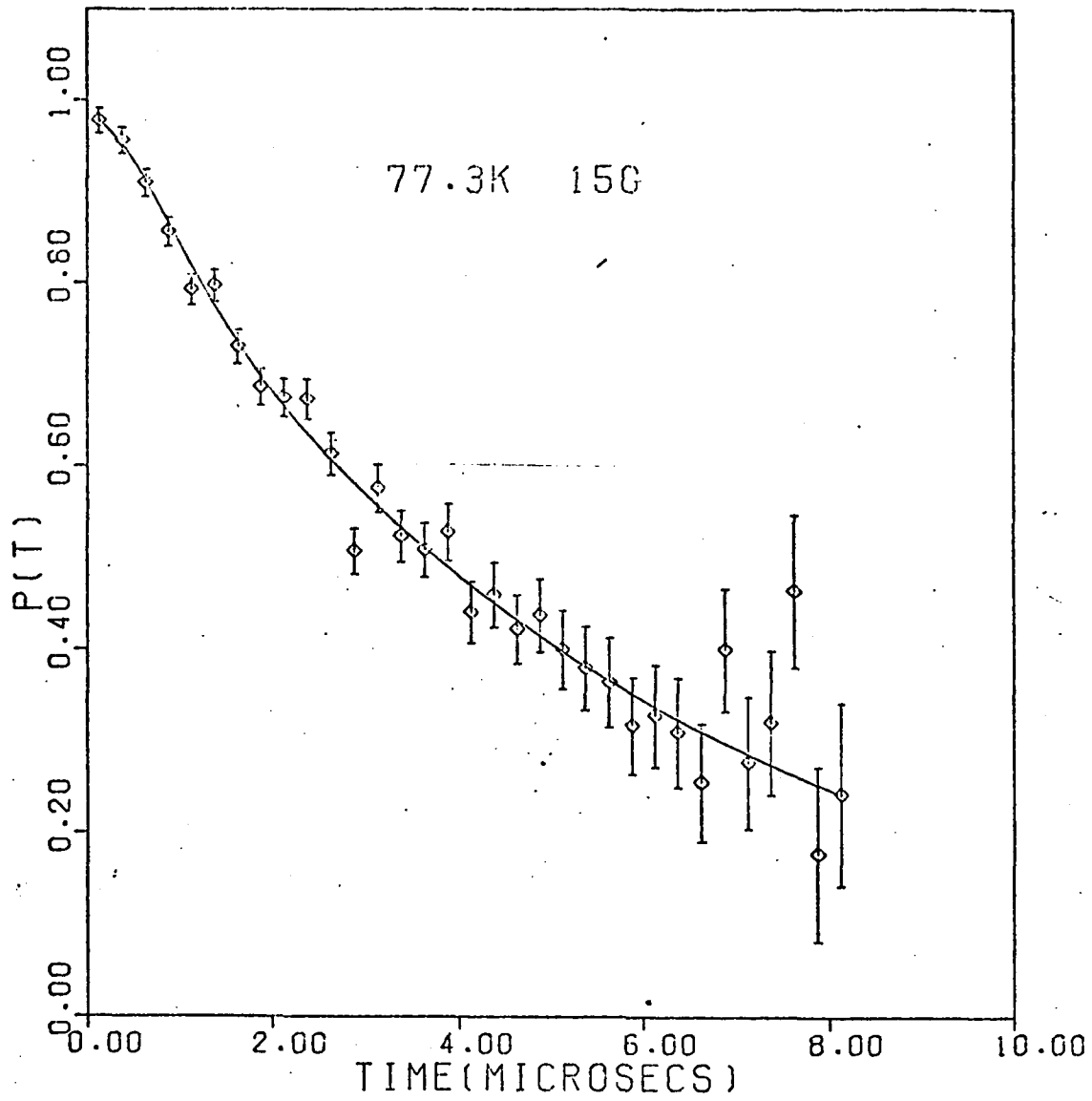


Fig. 27

Fig. 28

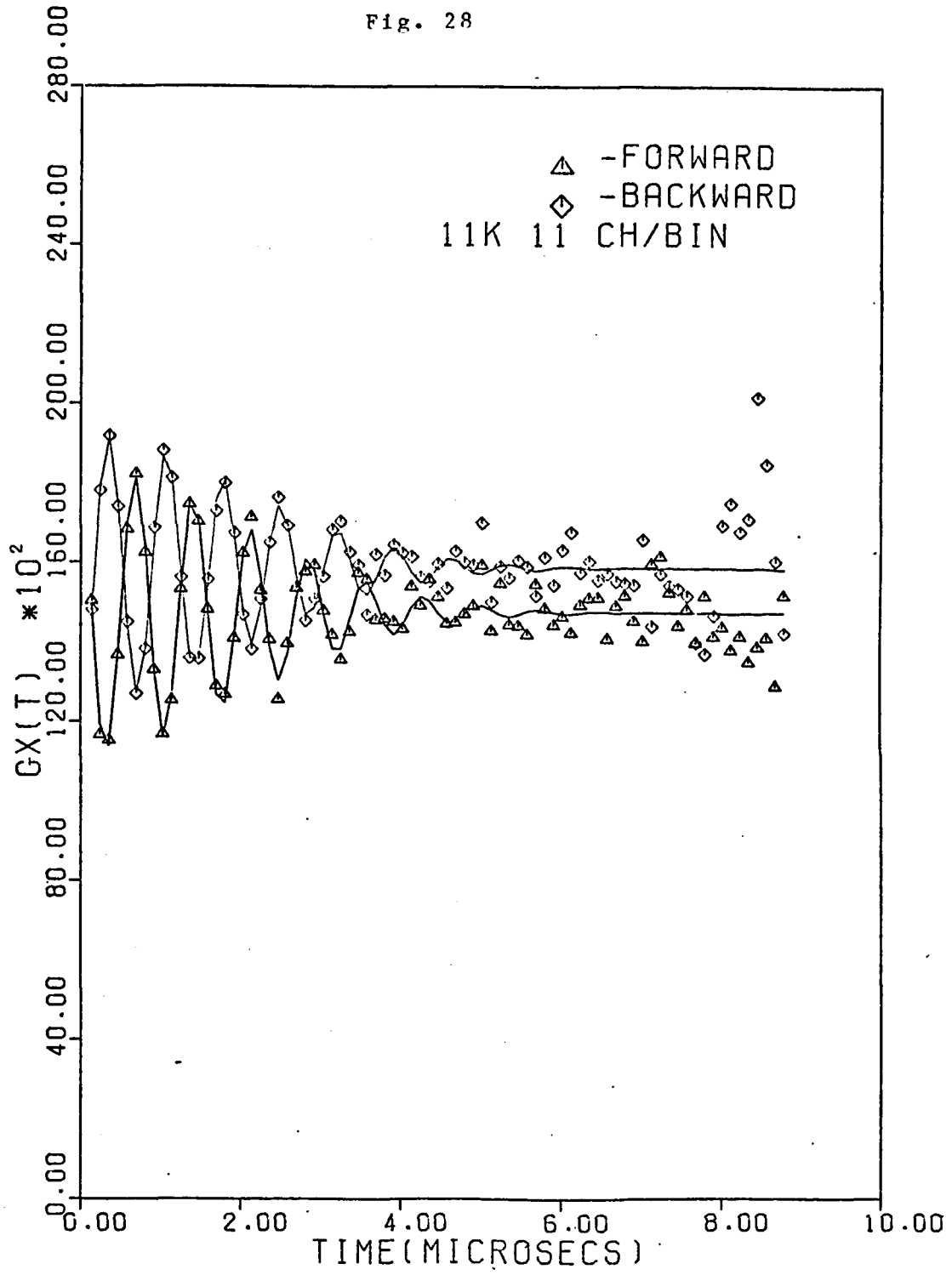


Fig. 29

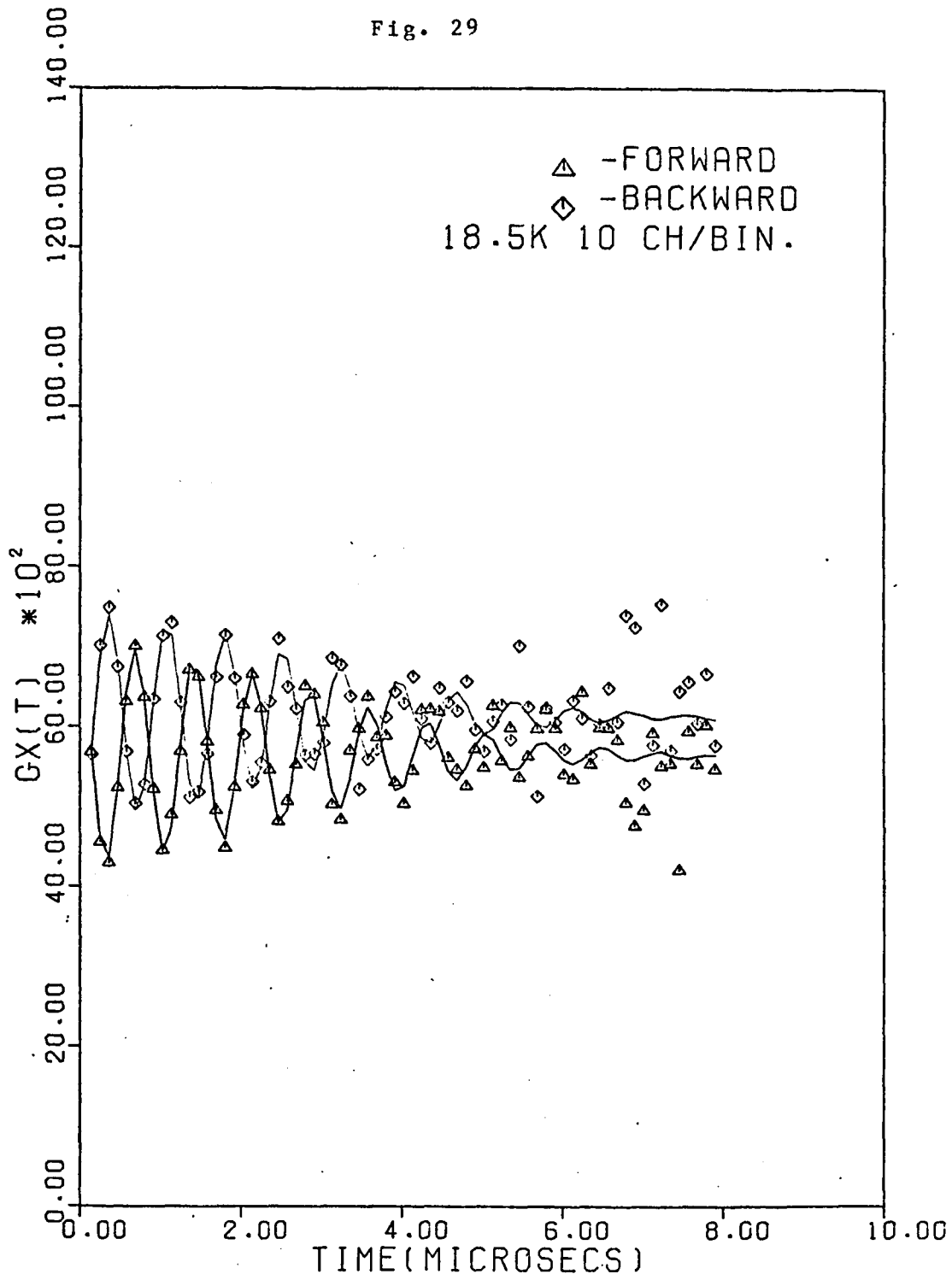


Fig. 30

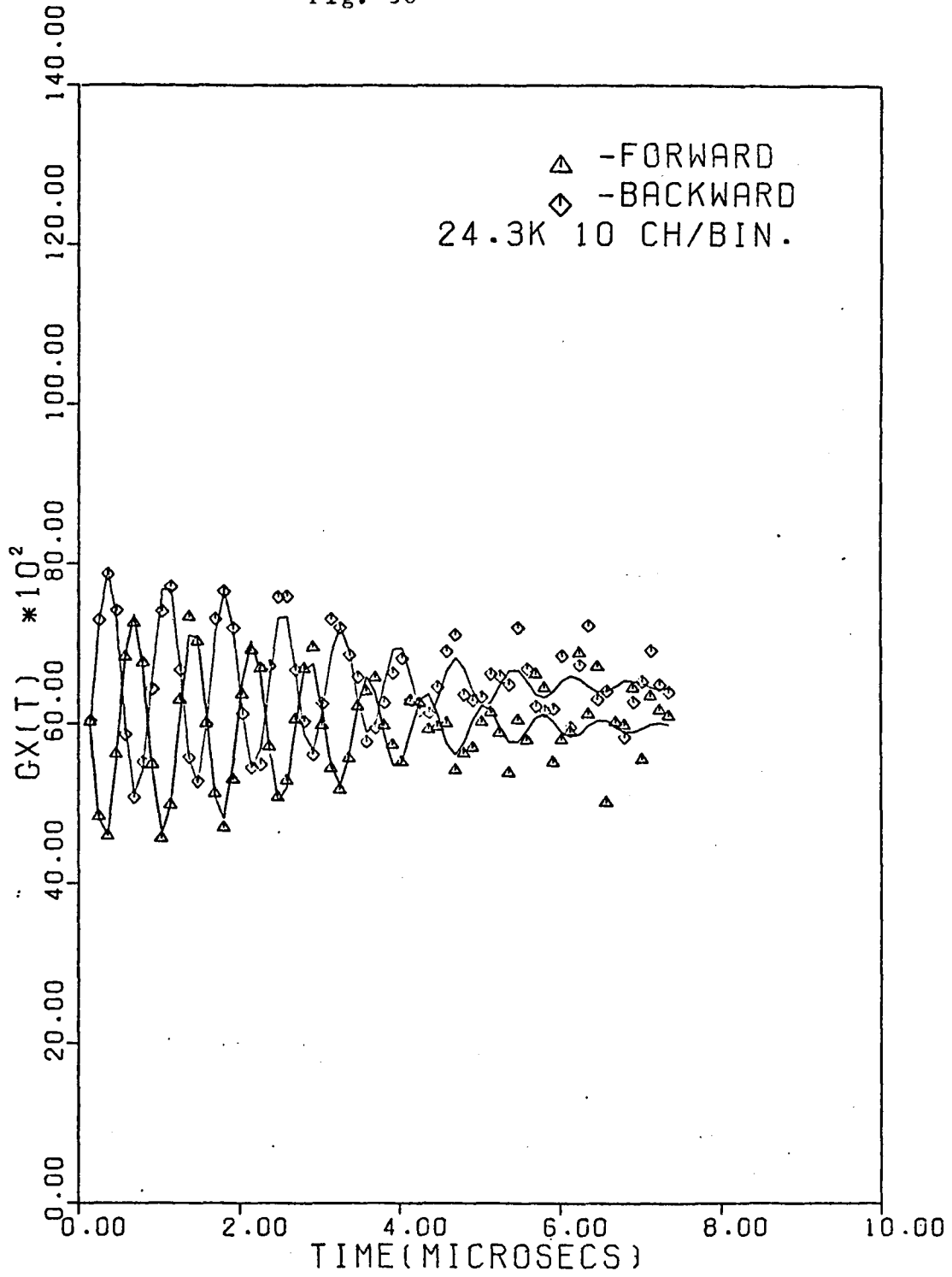


Fig. 31

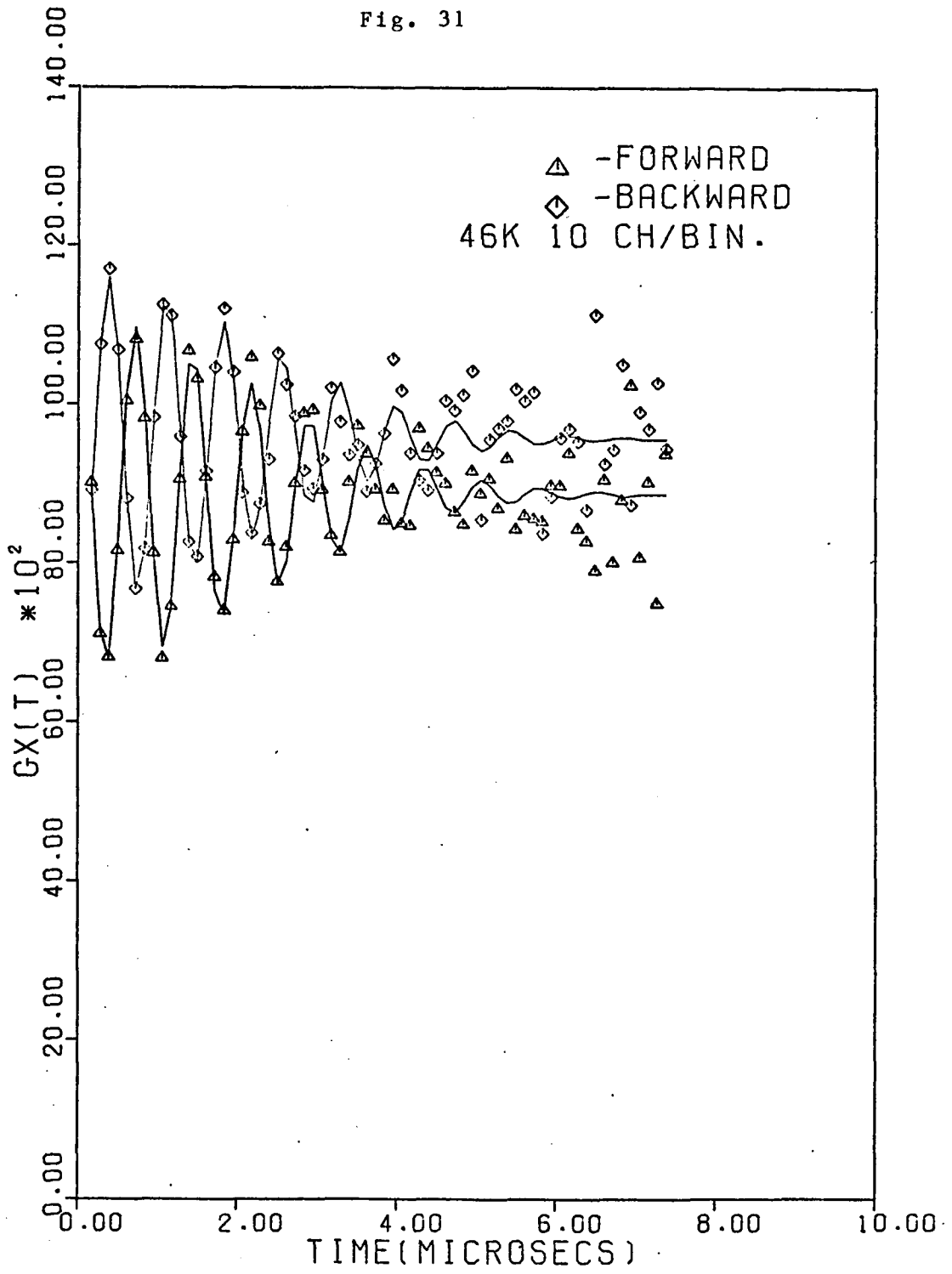
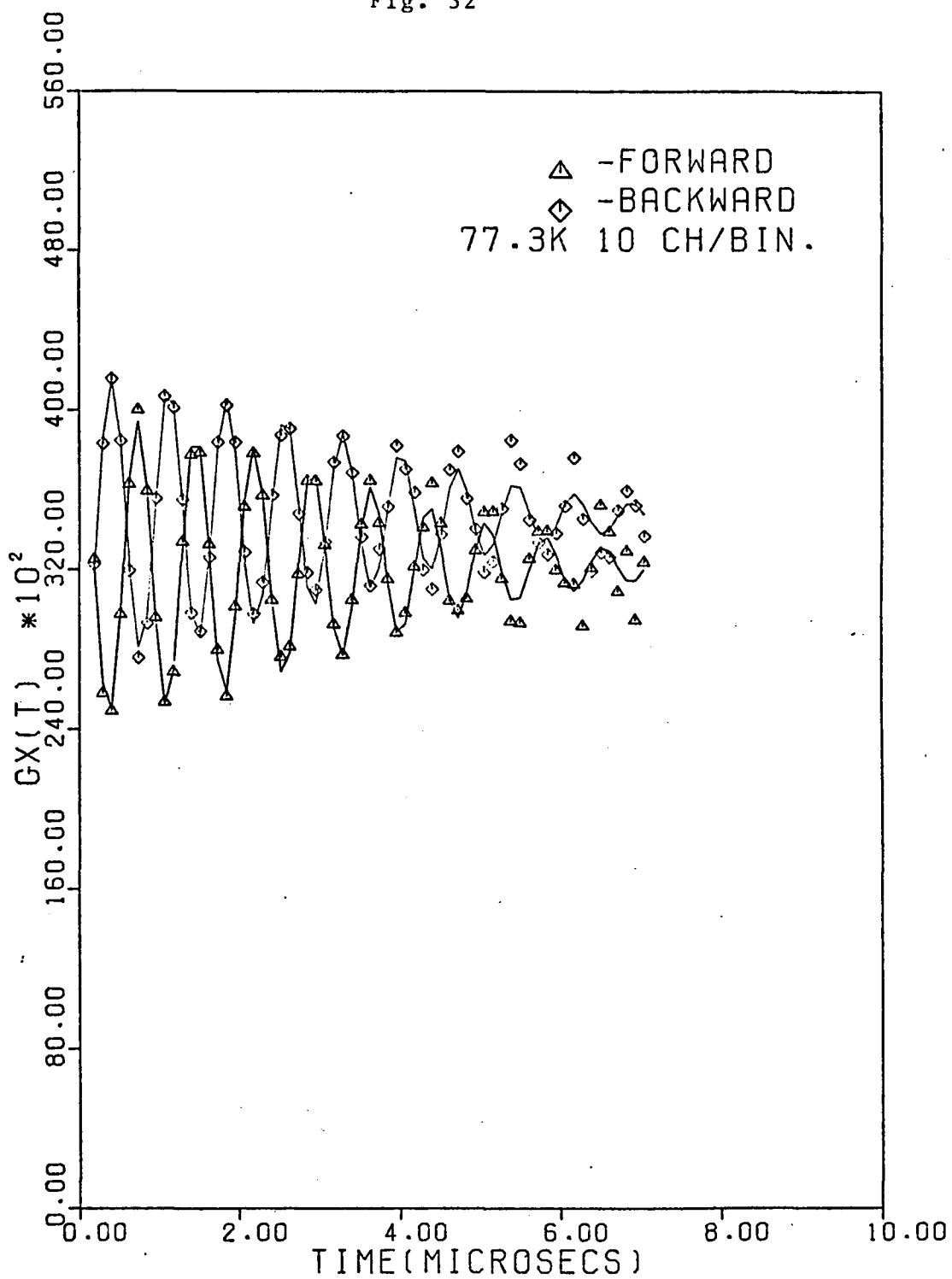


Fig. 32



AL(SI) 5 TRAPS FIT.

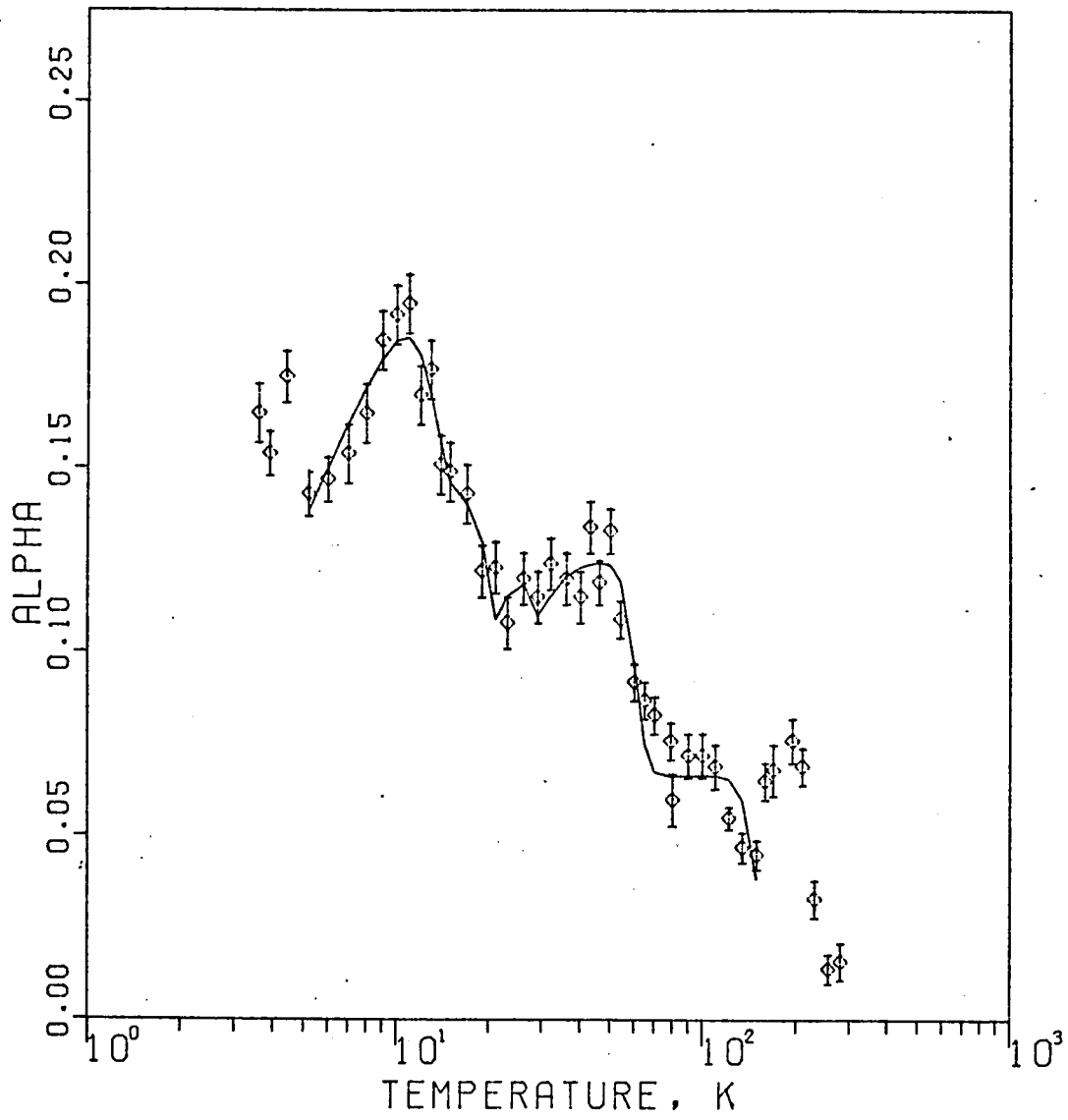


Fig. 33

AL(AG) 3 TRAPS

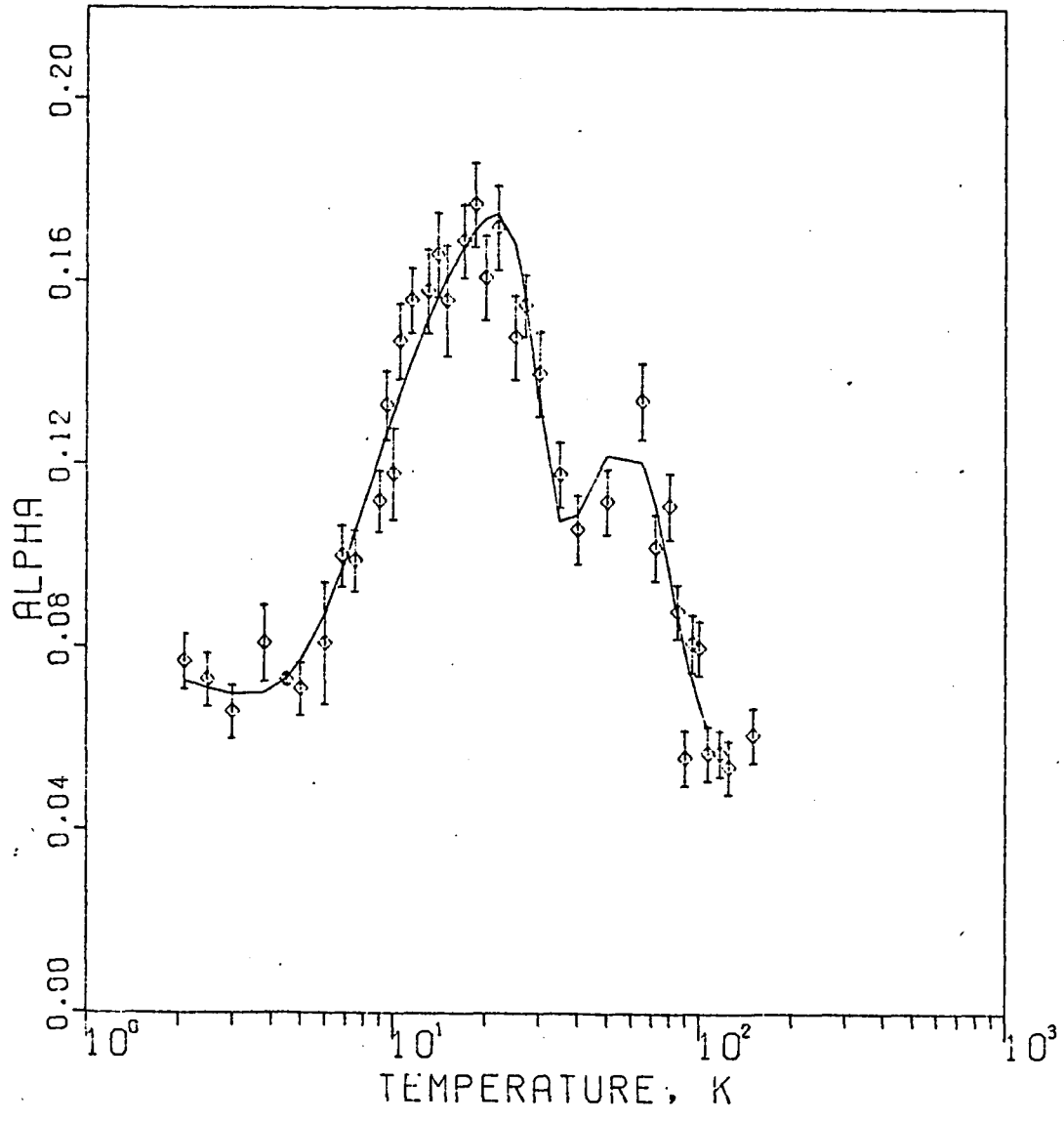


Fig. 34

AL(MG) 4 TRAPS B1 FIXED

